This is to certify that the
dissertation entitled

DISSOLUTION WEAR: DECOMPOSITION OF TOOL MATERIAL, AND CONCENTRATION PROFILE INTO CHIP

presented by

Tim Kong-Ping Wong

has been accepted towards fulfillment
of the requirements for the

Ph.D. degree in Materials Science and Mechanics

Major Professor's Signature

11/23/04

Date

DISSOLUTION WEAR: DECOMPOSITION OF TOOL MATERIAL, AND CONCENTRATION PROFILE INTO CHIP

By

Tim Kong-Ping Wong

A DISSERTATION

Submitted to
Michigan State University
in partial fulfillment of the requirements
for the degree of

DOCTOR OF PHILOSOPHY

Department of Materials Science and Mechanics

2004

ABSTRACT

DISSOLUTION WEAR: DECOMPOSITION OF TOOL MATERIAL, AND CONCENTRATION PROFILE INTO CHIP

By

Tim Kong-Ping Wong

The predictive capability of Kramer's theory of dissolution wear has raised questions as to whether dissolution or diffusion is the dominant mechanism underlying tool wear. The diffusion mechanism finds support in experimentation and modeling of mass transfer (e.g., the Molinari-Nouari model of the experimental findings of Subramanian et al.), and fits more naturally in the setting of the irreversibilities of turning processes. Kramer's dissolution mechanism, by contrast, is based on equilibrium thermodynamics. Our present aim is to re-phrase the dissolution hypothesis of tool wear as a boundary condition for species transfer within the chip's bulk via diffusion. In this setting, dissolution is defined as the combined events of tool decomposition at the interface and the subsequent mass transfer of decomposed elements into the chip region. A set of equations is constructed wherein the tool is treated as a mechanically rigid, but chemically active, thermal conductor; the chip is treated as a rigid-perfectly plastic, thermally conducting material; and the behavior of the frictional-contact interface between tool and chip is described by a weak coupling of thermal and mass transfer. Chemical equilibrium is invoked for the distribution of tool species at the tool-chip interface. The Frank-Turnbull mechanism of molecular reaction (between interstitial impurities and vacancies to form substitutional impurities) is used as a hypothesis to

explain the concentration profile of tool constituents into the chip as found by Subramanian et al. in 1993. The present interpretation of the Frank-Turnbull mechanism is illustrated by finite-element simulations. Physical parameters have either been estimated or curve-fitted to observed data, and the level of inexactness inherent in the curve-fit process limits the present work to a demonstration of only the sufficiency of the model. The assumptions made, their implications, parameters varied, and quantities calculated are summarized in the conclusion.

ACKNOWLEDGMENTS

I am deeply thankful for the factors that have collectively made this moment possible. My thanks go to my family and friends in California, who have been the foundation of everything I do; to the admissions committee at Michigan State, for giving me the opportunity to pursue my goal; to the professors from whom I have taken classes, for their honesty and energy; to the administrative staffs at the Department of Materials Science and Mechanics and the Department of Mechanical Engineering, for their consistent help that at times reach beyond what is required of them; to my friends in Michigan, for all of the intangibles; and to the professors on my dissertation committee, for their grace and generosity in giving constructive criticisms.

A semester of teaching assistantship that the Department of Materials Science and Mechanics has provided is gratefully acknowledged. The summer internship at NIST has been a treasured experience, not only from the point of view of learning and exploration, but also from the friendships that I have made. I have also benefited from the support of a unique organization—the Manufacturing Research Consortium at Michigan State University. My appreciation for what it has set out to accomplish is heart-felt, and I thank the organizers of the Consortium, as well as the sponsors who have visited our campus.

Most of all, I would like to thank Dr. Patrick Kwon, for so many things.

TABLE OF CONTENTS

Table of Contents (continued)

LIST OF TABLES

LIST OF FIGURES

List of Figures (continued)

Key to Variables, Parameters, and Operators

A, B : impurity and host material, respectively

A_i & A_s , B_V : interstitial & substitutional impurities, and host vacancies, respectively

$\mathbf{b}$: body force per unit mass (N/kg)

$\mathbf{b}_k$: body force per unit mass for species k ‡

c : total concentration of all species (mol/m^3)

c_k : molar concentration of species k ‡

$\hat{c}_v$: mass-based specific heat at fixed volume (J/(kg·K)

$\hat{c}_{work}$: workpiece $\hat{c}_v$ (work & chip), 0th-order problem

$\hat{c}_{tool}$: tool $\hat{c}_v$, 0th-order problem

C_{ij} : ij-th component of the advection matrix in the 0th-order problem

$\mathbf{D}$: rate of deformation (1/s)

D_k : diffusivity, within iron, of species k (m^2/s) ‡

DOF: number of nodes in the 0th-order problem

f_k : rate of mass generation of species k per unit volume (kg/(m^3·s)) ‡

F_k : (e.g., F_s , $F_{V,psz}$) rate of mole generation of species k per unit volume (mol/(m^3·s)) ‡

F_{ij} : ij-th component of the effective flux-coupling matrix in the 0th-order problem

F_{cut} , F_{feed} , F_{shear} , F_{rake} : cutting forces for the 0th-order problem (N)

$\hat{g}_1$, $\bar{g}_1$: 1st-order Gibbs free energy (see Notes)

$\Delta\bar{g}_{activn}$: change in molar Gibbs free energy of chip-boundary activation (J/mol)

$\Delta\bar{g}_{decomp}$: change in molar Gibbs free energy of tool decomposition

G : Gibbs free energy (J)

h : heat-transfer coefficient (W/(m^2·°C))

h_i : bilinear shape function over node i

I : the union of the rake and flank interfaces

$\mathbf{j}_k$: diffusive mass flux for species k ‡ with respect to $\mathbf{v}$

$\mathbf{J}_k$ *: diffusive molar flux of species k ‡ with respect to $\mathbf{v}$*

k : thermal conductivity (W/(m·K))

k_{work} : workpiece thermal conductivity (work & chip) for the 0th-order problem

k_{tool} : tool thermal conductivity for the 0th-order problem

k_{fwd} : rate constant for the forward Frank-Turnbull reaction (1/s)

k_{diss} : rate constant for interfacial dissolution

k_V : rate constant for vacancy production

K_{ij} : ij-th component of the thermal-conduction matrix, 0th-order problem

l_{diss} : length scale for interface dissolution (m)

L, L_{work} , L_{tool} : length of the work or tool element in the one-dimensional heat-transfer example

L_{rake} : tool-chip contact length along rake (m)

m : total mass of all species (kg)

m_k : mass of species k ‡

M_k : molecular weight of species k (kg/mol) ‡

M_{ij} : ij-th component of the heat-capacity matrix, 0th-order problem

N : total number of species

p_0 : 0th-order pressure (N/m^2)

$\mathbf{q}$: heat flux (J/(m^2·s))

$\mathbf{q}_0$, $\mathbf{q}_1$: 0th- and 1st-order heat fluxes

q_{flank} , q_{rake} : heat fluxes along the flank and rake interfaces, 0th-order problem

Q_i : i-th component of effective external forcing in the 0th-order problem (W/m)

Q: interfacial heat flux in the one-dimensional heat-transfer example

Q_{w1} , Q_{w2} : end-node heat fluxes for the work, one-dimensional heat-transfer example

Q_{t1} , Q_{t2} : end-node temperatures for the tool, one-dimensional heat-transfer example

r : rate of heat generation per unit mass (W/kg)

r_{work} : rate of heat generation within the primary shear zone, 0th-order problem

R : universal gas constant (cal/(mol·K))

R_i : i-th component of effective internal forcing in the 0th-order problem (W/m)

t : time (s)

t1, t2: end nodes of the tool in the one-dimensional heat-transfer example

t_{ij} : ij-th component of tool 'stiffness' matrix, one-dimensional heat-transfer example

$\mathbf{T}$: Cauchy stress (N/m^2)

u, $\hat{u}$, $\bar{u}$: internal energy (J/#) (see Notes)

Key to Variables, Parameters, and Operators (continued)

$\hat{u}_0$, $\hat{u}_1$, $\overline{u}_1$: 0th- and 1st-order internal energies (see Notes)

$\mathbf{v}$: mass-averaged velocity (m/s)

$\mathbf{v}_k$: velocity of particles of species k ‡

$\mathbf{v}^*$: concentration-averaged velocity

v_x, v_y : horizontal and vertical workpiece velocities, 0th-order problem

v_{cut}, v_{feed}, v_{shear}, v_{rake} : cutting speeds for the 0th-order problem

V, $\hat{V}\left(=\rho^{-1}\right)$, $\overline{V}$: volume (see Notes)

w : Galerkin weighting function

w1, w2 : end nodes of the workpiece in the one-dimensional heat-transfer example

w_{ij} : ij-th component of workpiece 'stiffness' matrix, one-dimensional heat-transfer example

W : width of system transverse to flow (m)

x : horizontal coordinate (global or local)

X_k (i.e., X_i, X_s, X_V): mole fraction of species k $(=c_k / c)$ ‡

$X_{k,eq}$: solubility, within iron, of species k ‡

$X_{Co,eq}$: solubility of cobalt in iron

$X_{W,eq}$: solubility of tungsten in iron

y : vertical coordinate (global or local)

Y_k : mass fraction of species k $(=m_k / m)$ ‡

α: fraction of impurities within the chip lattice identified as interstitial impurities

β: fraction of heat partitioned to the workpiece interface, 0th-order problem

η, $\hat{\eta}$: entropy (J/(K·#)) (see Notes)

$\hat{\eta}_0$, $\hat{\eta}_1$: 0th- and 1st-order entropies (see Notes)

φ: fraction by which the tungsten solubility is multiplied to obtain the effective solubility of cobalt in iron during dissolution

ν_{Fe} : Debye frequency of iron lattice

ρ: average density (kg/m^3)

ρ_k : density of species k ‡

ρ_{work} : workpiece (work & chip) density, 0th-order problem

ρ_{tool} : tool density, 0th-order problem

θ : temperature (K or °C)

θ_0, θ_1 : 0th- and 1st-order temperatures

θ_j : j-th node temperature, 0th-order problem

θ_{work} : workpiece (work & chip) temperature, 0th-order problem

θ_{tool} : tool temperature, 0th-order problem

θ_{w1}, θ_{w2} : end-node temperatures for the work, one-dimensional heat-transfer example

θ_{t1}, θ_{t2} : end-node temperatures for the tool, one-dimensional heat-transfer example

ψ, $\hat{\psi}$: Helmholtz free energy (see Notes)

$\hat{\psi}_0$, $\hat{\psi}_1$: 0th- and 1st-order Helmholtz energies

Δ	difference operator
∇	spatial gradient
$\nabla\cdot$	spatial divergence
$\nabla\cdot\nabla$	Laplacian
$\partial(\cdot)/\partial t$	partial derivative with respect to time
$D(\cdot)/Dt$	total (or material) derivative with respect to time

$\mathbf{T}_1 : \mathbf{T}_2 = \text{trace}\left(\mathbf{T}_1^{\mathrm{T}}\mathbf{T}_2\right)$, tensor product

$(\nabla : \mathbf{T})\cdot\mathbf{c} = \nabla\cdot\left(\mathbf{T}^{\mathrm{T}}\mathbf{c}\right)$, divergence of a tensor $\mathbf{T}$, where vector $\mathbf{c}$ is any constant vector

‡ Index k takes on the values of 'i', 's', or 'V', denoting 'interstitials', 'substitutionals', or 'vacancies', respectively, within the chip lattice in the 1st-order (species transfer) problem.

Notes: Extensive quantities such as volume V, internal energy u, entropy η, etc., are written on either a mass or mole basis. For uniformity in notation, an overhead caret (e.g. $\hat{u}$) is used to denote a quantity per unit mass, whereas an overhead bar is used to denote a quantity per unit mole (e.g. $\overline{u}$). Following standard notation, partial molar quantities is denoted by a subscript indicating the particular species (e.g., $\overline{u}_\alpha = \partial u / \partial n_\alpha$). The '#' symbol denotes a wild-card unit that could either be kg or mol depending on whether a quantity is expressed on a per-unit-mass or per-unit-moles basis. Quantities that are treated in the numerical simulations as material constants are not italicized (e.g., thermal conductivity, k).

INTRODUCTION

Dissolution as a high-temperature wear mechanism has first been proposed by Kramer [1979]. The key idea is to interpret the solubility of a tool material within the work piece as a measure of the tendency for dissolution. A condition of chemical equilibrium involving free energies [Kramer, 1979; Kramer and Suh, 1980], namely,

$$\Delta G_{\text{decomposition of tool}} = \Delta G_{\text{dissolution of tool components into work}}$$

is introduced to estimate values of solubility. In this context, 'dissolution' is taken as the placement of tool components into the work. Further, a simple argument relates the solubility to the volumetric wear rate up to an unknown (but assumed common) multiplicative factor, which enables the life expectancy of different tool materials to be compared on a relative basis. The quantitative results not only conform to common experience, but also identify certain nitrides and oxides for their dissolution-wear resistance at high-temperatures. Hence, in contrast to the theories at the time that favor the non-equilibrium mechanism of diffusion [Cook and Nayak, 1966; Naerheim and Trent, 1977], the importance of an equilibrium quantity, namely the solubility, is thrust to the fore.

Over 20 years after the seminal work of Kramer, the actual concentration profiles of tool constituents dissolved into the chip have been measured and reported by Subramanian, Ingle and Kay [1993]. Their data, which correspond to the machining of

an AISI 1045 steel using a tungsten-carbide tool with cobalt binder (WC-Co), are reproduced in Figure 1:

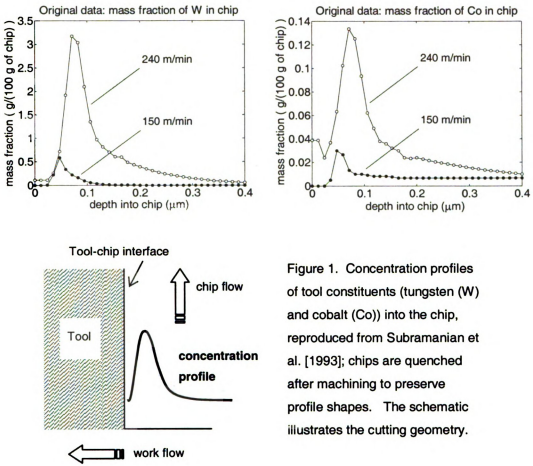

Figure 1. Concentration profiles of tool constituents (tungsten (W) and cobalt (Co)) into the chip, reproduced from Subramanian et al. [1993]; chips are quenched after machining to preserve profile shapes. The schematic illustrates the cutting geometry.

According to the authors, the humped distribution may be due to the formation of a dislocation channel close to the contact interface. As seen from Figure 1, such a dislocation channel would have a width of about 1/10 of a micron and is located about 1/10 of a micron away from the tool-chip interface; this is compared with a total depth of a chip that measures hundreds of microns. As the regions adjacent to the primary and secondary shear zones also experience severe shear deformation, it is not easy to see why the dislocation channel is so precisely narrow in its appointed location. Solubility alone cannot explain the humped distribution either, for a humped solubility profile would

require a humped temperature profile away from the interface, which stands in contrast with an exponentially decaying behavior that is well known (see also Chapter 2).

Using a set of coupled, reaction-diffusion equations, Giese, Stolwijk and Bracht [2000] have shown that a humped profile of copper and nickel impurities diffusing in a germanium lattice can be explained by the Frank-Turnbull mechanism of molecular mass transfer [Frank and Turnbull, 1956; Sturge, 1959]. Delaying the discussion of this mechanism until later, it suffices to say that the enabling idea is to derive a humped distribution as the product of a decaying function and an increasing function, as the following example illustrates:

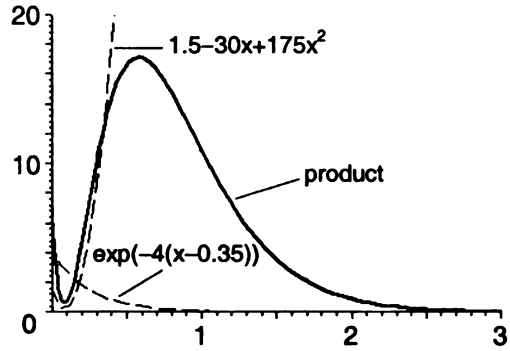

Figure 2. Example of humped distribution with arbitrarily chosen functions

We use the same idea to capture the data of Subramanian et al. The reaction-diffusion equations of Giese et al. are supplemented with a simplified model of advection to describe mass transfer in the presence of chip flow. An exponentially decaying, interstitial profile is obtained by solving an advection-diffusion equation, while an increasing vacancy distribution is chosen so that its product with the interstitial decay—under the requirement of mass conservation of the Frank-Turnbull reaction—fits the experimental data. The result is an interpretation of the humped profile via the Frank-Turnbull mechanism. The role of chip flow is to establish thermal equilibrium, and to

transport the vacancies created in the primary shear zone directly into the chip, where they interact with the tool interstitials in the proposed Frank-Turnbull reaction; this is summarized in Figure 3.

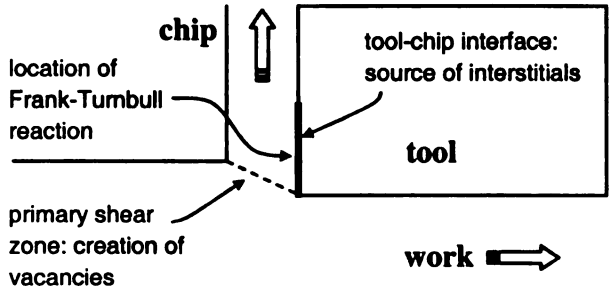

Figure 3. Sources for and location of the Frank-Turnbull reaction

Kramer's original idea on solubility [Kramer, 1979] is re-interpreted within the context of the rate constant of dissolution, which in turn enters the boundary conditions of the proposed advection-diffusion-reaction equations. It is postulated that the boundary flux of dissolved components across the tool-chip interface is proportional to the available solubility; the mole fraction of decomposed tool constituents; and the mole fraction of vibration-activated openings on the chip surface that are wide enough to admit tool constituents (also called "activation complexes"). A similar rate expression has been discussed by Suh [1986, p. 369], which is less restricted than the present one in that in Suh's expression, the idea of activation complexes is not needed. In the present interpretation, dissolution is defined as the combined events of the decomposition of tool constituents at the interface, and the absorption of these constituents by the chip. That diffusive mass transfer does not account for the entirety of tool wear can also be motivated from the profile data of Subramanian et al.; this idea is introduced in Section 3.4 and re-visited in light of the present results in Section 3.5.4.

The equations of mass transfer are incorporated into the balance laws of mechanics in a simplified way. First, the balances of mass and linear momentum are satisfied using a chosen advection field and a simple force balance (i.e., classical machining theory). Second, the balance of energy is decomposed additively into a zeroth-order problem governing the background temperature, and a first-order problem governing the mass transfer from the tool into the chip. The additive decomposition of energy is based on the large difference in time needed to achieve a steady state for thermal diffusion versus mass diffusion (Section 1.2). Bridgman's notion of generalized entropy [Bridgman, 1950] gives an operational meaning of temperature that appears in the energy equation (Section 1.1).

The general organization of the dissertation is as follows. Chapter 1 contains a review of the coupled governing equations and an explanation of the decomposition into the temperature problem and the species-transfer problem. In Chapter 2, the temperature background problem is solved. Chapter 3 contains the main results of the dissolution-wear problem as stated before, including a discussion of the non-uniqueness of the Frank-Turnbull representation, and a brief survey of experimental methods that are available for measuring the spatial distribution of vacancies. Lastly, Chapter 4 is a summary of results.

Chapter 1

THERMOMECHANICS OF TOOL AND CHIP WITH MASS TRANSFER

A model of particle exchange from one region to another in the presence of bulk motion and deformation involves a sizable number of coupled equations. However, for the high-temperature phenomenon of dissolution considered here, we place focus on the solution for the temperature field and the tracking of species exchange, while those equations associated with the purely mechanical aspects are only approximately satisfied. The result will be a set of equations involving advection, diffusion, and reaction (Chapters 2 and 3).

1.1. The fully coupled equations

The tool is treated as a mechanically rigid, but chemically active, thermal conductor, and the only equation of concern is the energy equation, or Equation (p) of Table 1 written for the tool variables. For the tool, the stress power $\mathbf{T} : \mathbf{D} = \mathbf{0}$ because of rigidity. The chip is treated as a rigid-perfectly plastic, thermally conducting material, and all equations of Table 1 are applicable. In the present approach, the thermodynamics of the cutting process is not predicated on the accessibility of states via reversible processes, from which entropy is constructed. Instead, by appealing to the recoverability—via a hysteresis process—of any point in a perfectly plastic process, a generalized entropy is postulated to be a state function [Bridgman, 1950]. Further, by

arguing that the material's structure is unchanged by planes of perfect slip, a generalized, system entropy is chosen to be the same one that is used for a material that is rigid at all locations except planes of perfect slip. Irreversibility is indicated by a 100% conversion of the plastic work into heat; in other words, $\mathbf{T} : \mathbf{D}$ is treated as a heat-source term, and strain does not enter explicitly as an argument of the energy functions. The escaped heat from plastic work adds to the entropy of the surrounding material, and is the basis through which an absolute temperature of the system is prescribed in the presence of perfectly plastic deformation. Such a temperature is precisely the same one that enters the energy equation (θ of Equation (p), Table 1).

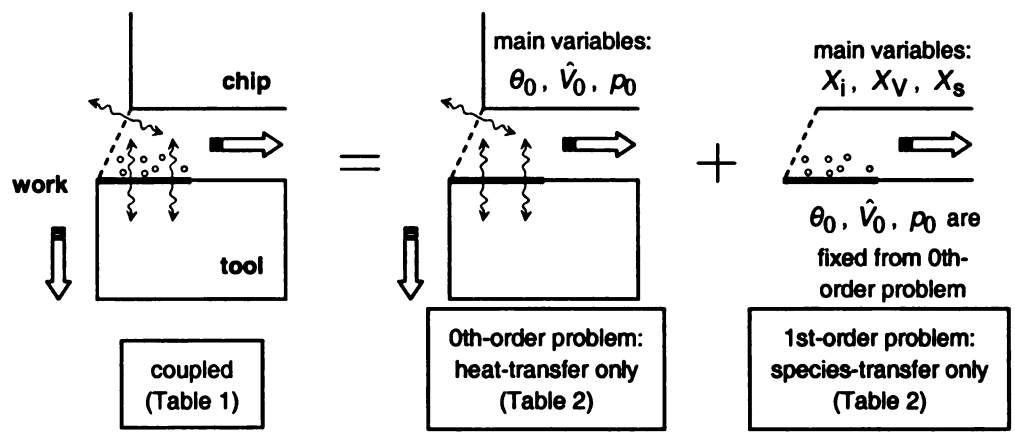

Figure 4. Decomposition of fully coupled equations

Table 1 summarizes the governing equations of the fully coupled problem. For discussion and derivation of the equations, the reader is referred to the references [Mase and Mase, 1999, Ch. 5; Bird et al., 2002, Ch. 19]. In spite of the numerous equations, Figure 4 shows the simplification that an additive decomposition brings and the key variables that are of interest. This decomposition is justified in the next section.

Table 1. Fully Coupled Equations

Overall mass continuity: $\frac{\partial \rho}{\partial t} + \nabla \cdot (\rho \mathbf{v}) = 0$ (a)

Incompressibility: $\nabla \cdot \mathbf{v} = 0$, $\frac{D\rho}{Dt} = 0$, or ρ is constant (b)

Average density: $\sum_k \rho_k = \rho$ (c)

Mass-averaged velocity: $\sum_k (\rho_k \mathbf{v}_k) = \rho \mathbf{v}$ (d)

Total flux for k-th species: $\rho_k \mathbf{v}_k$ (e)

Diffusive flux for k-th species: $\mathbf{j}_k = \rho_k (\mathbf{v}_k - \mathbf{v})$ (f)

Species continuity: $\begin{cases} \frac{\partial \rho_k}{\partial t} + \nabla \cdot (\rho_k \mathbf{v}_k) = f_k, \text{or} \\ \rho \frac{DY_k}{Dt} + \nabla \cdot \mathbf{j}_k = f_k \end{cases}$ (g)

Consistency of mass continuity: $\sum_k f_k = 0$ (h)

Momentum balance: $\nabla : \mathbf{T} + \rho \mathbf{b} = \rho \dot{\mathbf{v}}$ (i)

Plasticity: elasticity ignored; $\mathbf{T} : \mathbf{T} = \sigma_y^2$ at yield and during loading (j)

Energy: $\rho \frac{D\hat{u}}{Dt} = \rho r - \nabla \cdot \mathbf{q} + \mathbf{T} : \mathbf{D} + \sum_k \mathbf{j}_k \cdot \mathbf{b}_k$ (k)

Assumption: $\mathbf{b}_k = \mathbf{0}$ (l)

Existence of entropy: $\hat{\eta} = -\frac{\partial \hat{\psi}(\theta, Y_1, ..., Y_{N-1})}{\partial \theta}$ (m)

Helmholtz free energy: $\begin{cases} \psi = \psi(\theta, m_1, ..., m_N) = \hat{\psi}(\theta, mY_1, ..., mY_N) = m \cdot \hat{\psi}(\theta, Y_1, ..., Y_N) = m \cdot \hat{\psi}(\theta, Y_1, ..., Y_{N-1}) \\ = m \cdot (\hat{u} - \theta \hat{\eta}) \end{cases}$ (n)

Entropy: $\rho \theta \frac{D\hat{\eta}}{Dt} = -\nabla \cdot \mathbf{q} + \mathbf{T} : \mathbf{D} - \rho \sum_{k=1}^{N-1} \frac{\partial \hat{\psi}}{\partial Y_k} \frac{DY_k}{Dt}$ (o)

Energy/First Law: $\rho \hat{c}_v \frac{D\theta}{Dt} = -\nabla \cdot \mathbf{q} + \mathbf{T} : \mathbf{D} + \sum_{k=1}^{N} \left\{ \frac{\bar{u}_k}{M_k} \cdot [(\nabla \cdot \mathbf{j}_k) - f_k] \right\}$ (p)

Second Law: $\rho \frac{D\hat{\psi}}{Dt} + \rho \hat{\eta} \frac{D\theta}{Dt} - \mathbf{T} : \mathbf{D} = (\rho r - \nabla \cdot \mathbf{q}) - \rho \frac{D\hat{\eta}}{Dt} \theta \le 0$ (q)

Constitutive law for heat transfer: $\mathbf{q} = -\mathbf{k} \nabla \theta + \sum_{k=1}^{N} \frac{\bar{u}_k}{M_k} \mathbf{j}_k$ (r)

Table 2. Weakly Coupled Equations

Zeroth-order problem (background temperature):

Overall mass continuity and incompressibility: steady flow fields uniform in the work region and in the chip region are prescribed. (a)

Momentum balance: satisfied on an integral basis via classical machining theory. (b)

Heat flux: $\mathbf{q}_0 = -\mathrm{k}\nabla\theta_0$ (c)

Energy: $\rho\dfrac{D\hat{u}_0(\theta_0)}{Dt} = -\nabla\cdot\mathbf{q}_0 + \mathbf{T}:\mathbf{D}$ (d)

Heating by cutting forces: $\int \mathbf{T}:\mathbf{D}dV = \int \mathbf{t}\cdot\mathbf{v}dA$ (e)

Helmholtz free energy: $\hat{\psi}_0(\theta_0) = \hat{u}_0 - \hat{\eta}_0\theta_0$ (f)

Entropy: $\rho\theta_0\dfrac{D\hat{\eta}_0(\theta_0)}{Dt} = -\nabla\cdot\mathbf{q}_0 + \mathbf{T}:\mathbf{D}$ (g)

Energy/First Law: $\rho\hat{c}_v\dfrac{D\theta_0}{Dt} = -\nabla\cdot\mathbf{q}_0 + \mathbf{T}:\mathbf{D}$ (h)

Second Law: $\rho\dfrac{D\hat{\psi}_0(\theta_0)}{Dt} + \rho\hat{\eta}_0\dfrac{D\theta_0}{Dt} - \mathbf{T}:\mathbf{D} \le 0$ (i)

First-order problem (mass transfer from tool to chip):

Weak coupling: $\theta_1 \equiv 0$; values of θ_0, $\hat{V}_0 = \rho^{-1}$, and pressure p_0 are fixed by zeroth-order problem. (j)

Total concentration: $\sum c_k = \mathrm{c}$ (k)

concentration-averaged velocity: $\sum(c_k\,\mathbf{v}_k) = \mathrm{c}\,\mathbf{v}^*$ (l)

Molar flux of k-th species: $c_k\,\mathbf{v}_k$ (m)

Diffusive molar flux of k-th species: $\mathbf{J}_k{}^* = c_k(\mathbf{v}_k - \mathbf{v}^*)$ (n)

Constitutive law for mass transfer: $\mathbf{J}_k{}^* = -D_k\,\nabla c_k$ (o)

Species continuity: $c\dfrac{DX_k}{Dt} + \nabla\cdot\mathbf{J}_k{}^* = F_k - X_k\sum_{m=1}^{N}F_m$ (p)

Heat flux: $\mathbf{q}_1 = \sum_{k=1}^{N}\dfrac{1}{\mathrm{M}_k}\dfrac{\partial u_1}{\partial n_k}\mathbf{j}_k = \sum_{k=1}^{N}\dfrac{\bar{u}_{1k}}{\mathrm{M}_k}\mathbf{j}_k$ (q)

Energy: $\rho\dfrac{D\hat{u}_1(Y_1,\ldots,Y_{N-1})}{Dt} = -\nabla\cdot\mathbf{q}_1$ (r)

Helmholtz free energy: $\hat{\psi}_1(Y_1,\ldots,Y_{N-1};\theta_0) = \hat{u}_1 - \hat{\eta}_1\theta_0$ (s)

Entropy: $\rho\theta_0\dfrac{D\hat{\eta}_1(Y_1,\ldots,Y_{N-1})}{Dt} = -\nabla\cdot\mathbf{q}_1 - \rho\sum_{k=1}^{N-1}\dfrac{\partial\hat{\psi}_1}{\partial Y_k}\dfrac{DY_k}{Dt}$ (t)

Energy/First Law: $0 = \rho\hat{c}_v\dfrac{D\theta_1}{Dt} = -\nabla\cdot\mathbf{q}_1 + \sum_{k=1}^{N}\left\{\dfrac{\bar{u}_{1k}}{\mathrm{M}_k}\cdot[(\nabla\cdot\mathbf{j}_k) - f_k]\right\}$ (u)

Second Law: $\rho\dfrac{D\hat{\psi}_1(Y_1,\ldots,Y_{N-1};\theta_0)}{Dt} \le 0$, or $\rho\dfrac{D\hat{g}_1(Y_1,\ldots,Y_{N-1};\theta_0,p_0)}{Dt} \le 0$ (v)

1.2. Weak coupling of the equations of plasticity and mass transfer

The reformulation of the fully coupled equations into two simpler problems is given in Table 2. These two problems correspond to decomposing the variables and functions $\{\theta,\hat{\eta},\hat{u},\hat{\psi},\mathbf{q}\}$ additively as follows:

$$\{\theta,\hat{\eta},\hat{u},\hat{\psi},\mathbf{q}\}=\{\theta_0,\hat{\eta}_0,\hat{u}_0,\hat{\psi}_0,\mathbf{q}_0\}+\{\theta_1,\hat{\eta}_1,\hat{u}_1,\hat{\psi}_1,\mathbf{q}_1\}, \tag{1}$$

where the subscript '0' refers to the zeroth-order problem of determining the background temperature, and the subscript '1' refers to the first-order problem governing molecular mass transfer. The motivation for this additive decomposition is that first, the rise in system temperature is almost entirely due to plastic deformation and friction, or equivalently, molecular mass transfer from the tool does not significantly affect the background temperature.[1] Second, for a given distance, the steady state for thermal diffusion is established much faster than the steady state for mass diffusion, which gives the decomposition (Equation (1)) a natural division in time scale. In fact, the thermal diffusivity of a material is typically orders of magnitude larger than the mass diffusivities of impurities moving through the material. For example, at 900°C and atmospheric pressure, the thermal diffusivity of iron is on the order of 10^{-6} m^2/s, whereas the mass diffusivities of cobalt and tungsten in iron is on the order of 10^{-14} m^2/s [Elliott et al., 1963, p. 690 for Co, p. 695 for W].

For the zeroth-order problem, the balance of mass and the balance of linear momentum (Equations (a) and (i) of Table 1) are satisfied by assigning a simple advection field and by balancing the cutting forces at steady state, as it is done in the

[1] The system temperature is significantly increased by drastic changes in the tool geometry due to wear, but this temperature increase is not due to mass-transfer coupling, but rather to changes in the cutting forces because of a change in tool geometry.

classical machining theory [Shaw, 1984]. The only use of plasticity is through an idealized, 100% conversion of plastic work and friction into heat. The rate of plastic work is connected to the cutting forces by the work-energy theorem, Equation (e) of Table 2. The conversion of cutting forces into friction power is discussed further in Chapter 2.

The first-order problem pertains to the small amount of mass transfer due to tool wear that is postulated to have no effect on the zeroth-order temperature and density fields. Hence, the quantities of interest are mass-transfer variations with respect to fixed background temperature θ_0 and specific volume $\hat{V} = \hat{V}_0$, as indicated in Table 2 (Statement (j)). Equilibrium distributions are governed by the Second Law, which is also expressed in terms of the Gibbs free energy $\hat{g}_1 = \hat{\psi}_1 - p_0\hat{V}_0$ (Inequality (v) of Table 2). The interfacial pressure p_0, which can be approximated from dividing the cutting forces by the contact area (the present work will not go farther than requiring an order-of-magnitude approximation), are those of the zeroth-order problem.

Additional relations in Table 2 (Equations (k) thru (q)) not found in Table 1 are discussed in [Bird et al., 2002, Chapter 19].

Chapter 2.

THE ZEROTH-ORDER PROBLEM FOR THE TEMPERATURE BACKGROUND

Because species transfer is so closely confined to a submicron region adjacent to the tool-chip interface, emphasis is placed on the details of the interfacial temperature distribution. However, the present calculations will also return the temperature field in a much wider region of the tool, work, and chip.

In turning processes, while a large portion of the contact interface between tool and work is under intimate contact [Zorev, 1958 (Fig. 54.7 on Plate 5); Wallace and Boothroyd, 1964 (Fig. 14, p. 84); Trent, 1967] (and hence temperature continuity holds), usually a distinct downstream region of gross, material deposition can be found [Doyle et al., 1979; Ackroyd et al., 2001; Kim and Kwon, 2001]. It is in this latter region of looser contact that a temperature jump is conjectured, even at steady state conditions. The aim is to find plausible conditions for a cooler work interface in orthogonal turning, as it pertains not only to chemical wear but to abrasive tool wear[2] as well.

From the solution of the heat equation, it is known that an interfacial temperature jump results if a convective-cooling condition is used with a heat transfer coefficient. Furthermore, the adiabatic condition and temperature continuity are two extremes of

---

[2] It is known that the hardness of metals and their inclusions decreases exponentially with increasing temperatures [Kramer and Judd, 1985]. In turn, abrasive wear has been shown to depend on the hardness ratio between tool and inclusions in the work material [Rabinowicz, 1977]. Abrasive wear intensifies if, during frictional contact, the temperature drops in going from tool to work material, as the inclusions in a cooler work material become effective abrasives.

behavior representing assignments of 0 and ∞ to the heat transfer coefficient, respectively. Here, the convective medium is the moving workpiece; however, the situation is complicated by the presence of friction. In fact, the amount of frictional heat that is partitioned to either side of the interface becomes an independent unknown. This is studied in the Appendix through the use of a 1D problem, where it is found that the heat-partition function enters directly into the expression for the interface-temperature jump (Equation (A23)). Because of the lack of exact solutions for complex flux conditions and geometry in 2D, results derived in the 1D example serve only as guidelines in the 2D FEM simulations. It is noted that the interface conditions considered are linear in the boundary temperature, as opposed to a non-linear condition, such as radiation, for which the present results do not apply.

While experimental proof of temperature jumps across frictional interfaces has yet been found, the results of the present study imply that *if* interfacial temperature jumps exist, then they can be characterized by the behavior of the heat-partition function across the interface. Assuming that temperature continuity is associated with intimate contact, the absence of intimate contact can then be quantified as deviations in the heat-partition function away from its value in the temperature-continuity case.

For an extensive coverage and review of analytical work on calculating temperatures in machining, and in particular, on the relationship between temperature continuity and heat partitioning, the reader is referred to a set of papers by Komanduri and Hou [2000; 2001a; 2001b]. The present discussion is largely motivated by the work of Chao and Trigger [1955; 1958]; here, we are interested in the opposite problem of how heat partitioning can be manipulated to achieve temperature jumps.

The subscript '0' denoting the zeroth-order problem is dropped for the remainder of this chapter.

2.1. Aim of 2D simulations

It will be seen that 2D simulation results are consistent with exact 1D results found in the Appendix. Namely, for the part of the contact interface where the convective-cooling condition is operative, if the heat partitioned to the work is less than that for the case of temperature continuity, then the work temperature will be cooler than the tool temperature (Inequalities (A24)). In turn, such a temperature jump will have ramifications for dissolution wear (Chapter 3).

2.2. Model and governing equations

The two dimensional geometry of concern is shown in the following figure, which corresponds to orthogonal turning with a 5° rake angle:

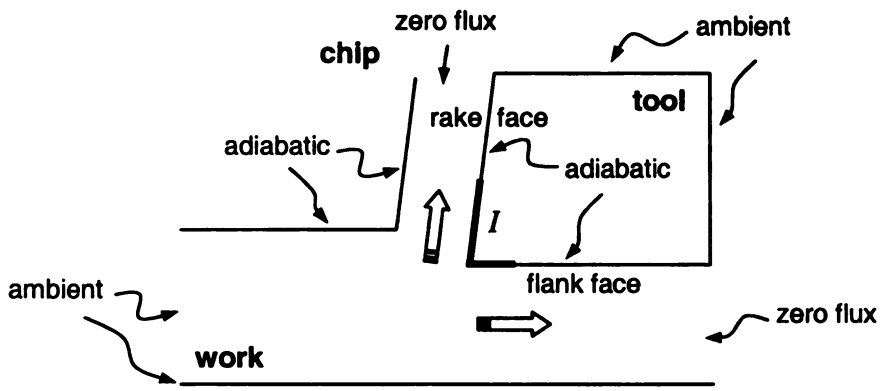

Figure 5. Schematic of cutting geometry; boundary conditions of heat transfer

The governing equations for the work and the tool temperatures are a re-phrasing of Equations (c) and (h) in Table 2 as follows:

$$\rho_{\text{work}}\hat{c}_{\text{work}}\frac{\partial\theta_{\text{work}}}{\partial t}=\left\{\begin{array}{l}k_{\text{work}}\left(\dfrac{\partial^2\theta_{\text{work}}}{\partial x^2}+\dfrac{\partial^2\theta_{\text{work}}}{\partial y^2}\right)\\ -\rho_{\text{work}}\hat{c}_{\text{work}}\left(v_x\dfrac{\partial\theta_{\text{work}}}{\partial x}+v_y\dfrac{\partial\theta_{\text{work}}}{\partial y}\right)+\rho_{\text{work}}r_{\text{work}}\end{array}\right\} \tag{2}$$

$$\rho_{\text{tool}}\hat{c}_{\text{tool}}\frac{\partial\theta_{\text{tool}}}{\partial t}=k_{\text{tool}}\left(\frac{\partial^2\theta_{\text{tool}}}{\partial x^2}+\frac{\partial^2\theta_{\text{tool}}}{\partial y^2}\right) \tag{3}$$

Here, x is the horizontal direction in Figure 5, y is the vertical direction, r is the rate of heating in the primary shear zone, k is the thermal conductivity, ρ is the density, $\hat{c}$ is the specific heat (per unit mass), v is the cutting speed, and θ is the temperature. Equations (2) and (3) are coupled through conditions at the contact interface (marked by the letter *I* in Figure 5). Boundary conditions are as follows. Infinitely far away from the cutting edge and contact interfaces, the system temperature returns to the ambient. Downstream of the contact interfaces along the rake and flank faces, adiabatic boundaries are assumed; that is, the bulk of the heat transfer is due to conduction across the contact interface *I*, and radiation far away from *I* does not play a key role. For the moving work and chip, the outflow boundary condition for the advection-diffusion equation is that of zero flux ($\mathbf{k}\cdot\text{grad}\theta=\mathbf{0}$), as discussed in the text of Zienkiewicz and Taylor [2000b, pp. 44-46].

The advection term in Equation (2),

$$\rho_{\text{work}}\hat{c}_{\text{work}}\left(v_x\frac{\partial\theta_{\text{work}}}{\partial x}+v_y\frac{\partial\theta_{\text{work}}}{\partial y}\right), \tag{4}$$

describes the flow of the work piece and its chip. For convenience, Equations (2) and (3) will be written in condensed form as

$$\rho\hat{c}\frac{\partial\theta}{\partial t}=k\nabla\cdot\nabla\theta-\rho c\mathbf{v}\cdot\nabla\theta+\rho r, \tag{5}$$

where it is understood that if the equation refers to the tool, then the velocity **v** is equal to **0**, and the internal source r equals 0, etc. The symbol ∇ denotes the spatial gradient.

Stress and strain fields are not direct inputs to the energy equation that is being considered. Instead, they enter through the rate of plastic work, which is considered as a heat-source term as stipulated in Chapter 1. In particular, the source term $\mathbf{T} : \mathbf{D}$ in Equation (h) of Table 2 is related to the external power through Equation (e) in Table 2. The basic inputs are forces[3] and velocities $\{ F_{\text{cut}}, v_{\text{cut}} \}$ and $\{ F_{\text{feed}}, v_{\text{feed}} \}$ in the cutting and feed directions, which can be resolved into $\{ F_{\text{shear}}, v_{\text{shear}} \}$ and $\{ F_{\text{rake}}, v_{\text{chip}} \}$ along directions tangent to the primary shear zone and the rake face, respectively [Shaw, 1984, pp. 21-22]. The heat generated in the primary shear zone is expressed as a body source

$$r_{\text{work}} = F_{\text{shear}} v_{\text{shear}}, \tag{6}$$

while the frictional heat generated along the secondary shear zone (tool-chip, or rake interface) is expressed as a boundary flux,

$$q_{\text{rake}} = (\mathbf{q} \cdot \mathbf{n})_{\text{rake}} = \frac{F_{\text{rake}} v_{\text{chip}}}{L_{\text{rake}} W}, \tag{7}$$

where **q** and **n** are the heat flux vectors and outward normal to the boundary, respectively, L_{rake} is the length of contact, and W is the out-of-plane thickness of the system. The frictional heat flux q_{flank} generated along the tertiary shear zone (tool-work, or flank interface) is also expressed as a boundary flux. As implied by DeVries'

[3] Knowing the cutting geometry and the cutting speeds, forces can be converted from specific-energy data that is tabulated in DeVries' text [1992, pp. 106-121] based on the classical machining theory. Here, we simply make use of the force and average-temperature data reported by Subramanian et al [1993].

text [1992, Figure 5.3c, p. 113], the product of q_{flank} and the flank-wear area can be obtained as the correction, in the presence of flank wear, to the total power input

$$F_{\text{cut}} v_{\text{cut}} + F_{\text{feed}} v_{\text{feed}}, \tag{8}$$

so that

$$\begin{aligned} q_{\text{flank}} &= (\mathbf{q} \cdot \mathbf{n})_{\text{flank}} \\ &= \frac{\{\text{change in } F_{\text{cut}} v_{\text{cut}} + F_{\text{feed}} v_{\text{feed}} \text{ due to flank wear correction}\}}{L_{\text{flank}} W}. \end{aligned} \tag{9}$$

The quantity F_{rake} in Equation (7) is calculated from F_{cut} and F_{feed} before the flank-wear correction is applied. The flux sources q_{rake} and q_{flank} are then uniformly applied to the contact regions regardless of whether they are prescribed to be temperature-continuous or convective-cooling.

The interface heat-transfer coefficient h is known to be highly dependent on process conditions. An intermediate value of h = 1000 W/(m^2·°C) is used in the simulations.[4]

2.3. Finite-element discretization

The finite-element weak form of the governing equations is derived by pre-multiplying Equation (5) (or Equations (2) and (3)) by a weight function w, integrating over the respective domains of work and tool, and performing integrations by part, resulting in

[4] As a crude indication, a value of h = 400 W/(m^2·°C) has been reported between molten aluminum and its die (http://msewww.engin.umich.edu/research/groups/pehlke/publications/lppm/index_html).

$$\int w\rho\hat{c}\frac{\partial\theta}{\partial t}dA = -\int(\nabla w)\cdot(k\nabla\theta)dA - \int w\rho c\mathbf{v}\cdot\nabla\theta\,dA + \int w\rho r\,dA + \int_I wk\nabla\theta\cdot\mathbf{n}\,ds \quad (10)$$

where $\int(\cdot)dA$ denotes area integration, and is taken over the entire areas of tool and work, and $\mathbf{n}$ is the outward normal vector to the boundary element ds. Because of the simplifying assumption that the boundaries of the system are mostly adiabatic, the boundary integral in the last term of Equation (10) include only the contribution from the contact interface I (rake and flank).

The finite-element approximation of the temperature field is

$$\theta \approx \sum_{j=1}^{DOF}\theta_j(t)h_j(x,y), \quad (11)$$

where DOF is the number of degrees of freedom—which, in the case of the scalar Equation (5), coincides with the number of nodes—and h_j is a bilinear interpolation function associated with the node j. Substituting approximation (11) into the weak form (10) using the Galerkin weighting

$$w(x,y) = h_i(x,y) \quad (12)$$

(i = 1,..., DOF), then performing the required integration DOF number of different times, results in the spatially discretized equation

$$\sum_j M_{ij}\frac{\partial\theta_j}{\partial t} = -\sum_j K_{ij}\theta_j - \sum_j C_{ij}\theta_j + R_i + Q_i + \sum_j F_{ij}\theta_j, \quad (13)$$

where the terms of Equation (13) are defined as follows:

$$\text{heat-capacity matrix } M_{ij} = \int\rho\hat{c}\,h_i h_j dA, \quad (13a)$$

$$\text{conduction matrix } K_{ij} = \int k\nabla h_i\cdot\nabla h_j dA, \quad (13b)$$

$$\text{advection matrix } C_{ij} = \int \rho c \mathbf{v} \cdot h_i \nabla h_j dA, \tag{13c}$$

$$\text{effective internal forcing } R_i = \int h_i \rho r_{\text{work}} dA, \tag{13d}$$

$$\text{effective external forcing } Q_i = \int_l h_i \mathbf{q} \cdot \mathbf{n} ds, \tag{13e}$$

$$\text{effective coupling-flux matrix } F_{ij} = \int_l h_i \left(k \nabla h_j - \mathbf{q}\right) \cdot \mathbf{n} ds. \tag{13f}$$

Flux conditions such as convective cooling and flux continuity enter into the matrix F_{ij}, the effect of which is to alter the "stiffness" matrix $K_{ij} + C_{ij}$. For the case of temperature continuity, the convective-cooling condition is irrelevant, and F_{ij} vanishes. The effective internal forcing R_i, which accounts for the power generated within the primary shear zone, is evenly distributed to a minimal set of nodes covering the primary shear zone at each stage of the mesh refinement. We will only study the steady state, so that the left-hand sides of Equations (5) and (10) vanish, and the nodal temperatures—θ_j in Equations (11) and (13)—become independent of time t. The $(k \nabla h_j - \mathbf{q})$ term in Equation (13f) isolates the contribution of gap heat transfer, as will be shown in a later example (Section 2.4.3).

The current algorithm makes use of the background material and source codes of Kwon and Bang [2000, Examples 5.9.1 and 6.6.2]. Alterations to the source codes are made to accommodate C_{ij}, F_{ij}, and the source term R_i. To improve accuracy in the present case of advection-dominated flow [Gresho and Lee, 1979] and for the modeling of the primary shear zone, a subroutine is written to incorporate the mesh-creation and mesh-refinement ('regular'/bisection) algorithms found in Matlab's "pde toolbox."

2.4. Implementing the interface conditions

A matrix equation in the form of Equation (13) for the steady state is written for each of the tool and work regions. Enforcement of interface conditions results in the coupling of the tool equation and the work equation. For a detailed discussion of such coupling, it is felt that the terminology of Equation (13) would unnecessarily obscure the essential ideas. Hence, in the following discussion, we use the notation of a 1D problem, and illustrate how different interfacial behavior can be implemented in the finite-element setting. For this purpose, we refer to Figure 6. The work and tool materials are schematically represented to lie along the x-axis, and they are in contact at the location shared by the work node w2 and the tool node t1:

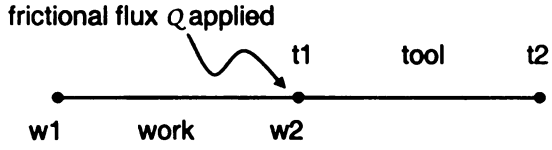

Figure 6: Ideal 1-D representation of the work and tool materials

A heat flux Q (in W/m^2) is applied at the interface. The energy equations governing the work and tool domains are

$$k_{work}\frac{d^2\theta_{work}}{dx^2}-\rho_{work}\hat{c}_{work}v\frac{d\theta_{work}}{dx}=0, \tag{14}$$

$$k_{tool}\frac{d^2\theta_{tool}}{dx^2}=0. \tag{15}$$

As before, k is the thermal conductivity, ρ is the density, $\hat{c}$ is the specific heat (per unit mass), v is the cutting speed, θ is the temperature, and x is the distance coordinate. The

system is subject to two far-field boundary conditions:

$$\theta_{\text{work}}\big|_{x=x_{\text{w1}}} = \theta_{\text{w1}} = 0, \tag{16}$$

and

$$\theta_{\text{tool}}\big|_{x=x_{\text{t2}}} = \theta_{\text{t2}} = 0, \tag{17}$$

For simplicity, one element is used to cover each of the work and tool regions. Then, the finite-element discretization of Equations (14) and (15) becomes

$$\begin{pmatrix} w_{11} & w_{12} \\ w_{21} & w_{22} \end{pmatrix}\begin{pmatrix} \theta_{\text{w1}} \\ \theta_{\text{w2}} \end{pmatrix} = \begin{pmatrix} Q_{\text{w1}} \\ Q_{\text{w2}} \end{pmatrix} \quad \text{and} \quad \begin{pmatrix} t_{11} & t_{12} \\ t_{21} & t_{22} \end{pmatrix}\begin{pmatrix} \theta_{\text{t1}} \\ \theta_{\text{t2}} \end{pmatrix} = \begin{pmatrix} Q_{\text{t1}} \\ Q_{\text{t2}} \end{pmatrix} \tag{18) \& (19}$$

where, for the work and the tool, respectively, w_{ij} and t_{ij} $(i, j = 1, 2)$ are components of the "stiffness" matrixes, $\theta_{\text{w}i}$ and $\theta_{\text{t}i}$ $(i = 1, 2)$ are the temperatures at nodes wi and ti, and $Q_{\text{w}i}$ and $Q_{\text{t}i}$ $(i = 1, 2)$ are corresponding components of the frictional heat fluxes, being positive for flux inflow into a region. Standard calculations for 1st-order, linear elements show that

$$\begin{pmatrix} w_{11} w_{12} \\ w_{21} w_{22} \end{pmatrix} = \begin{pmatrix} \dfrac{k_{\text{work}}}{L_{\text{work}}} - \dfrac{\rho_{\text{work}}\hat{c}_{\text{work}}v}{2} & -\dfrac{k_{\text{work}}}{L_{\text{work}}} + \dfrac{\rho_{\text{work}}\hat{c}_{\text{work}}v}{2} \\ -\dfrac{k_{\text{work}}}{L_{\text{work}}} - \dfrac{\rho_{\text{work}}\hat{c}_{\text{work}}v}{2} & \dfrac{k_{\text{work}}}{L_{\text{work}}} + \dfrac{\rho_{\text{work}}\hat{c}_{\text{work}}v}{2} \end{pmatrix}, \tag{20}$$

$$\text{and} \quad \begin{pmatrix} t_{11} t_{12} \\ t_{21} t_{22} \end{pmatrix} = \begin{pmatrix} \dfrac{k_{\text{tool}}}{L_{\text{tool}}} & -\dfrac{k_{\text{tool}}}{L_{\text{tool}}} \\ -\dfrac{k_{\text{tool}}}{L_{\text{tool}}} & \dfrac{k_{\text{tool}}}{L_{\text{tool}}} \end{pmatrix} \tag{21}$$

where $L_{\text{work}} = x_{\text{w2}} - x_{\text{w1}}$ and $L_{\text{tool}} = x_{\text{t2}} - x_{\text{t1}}$ are the element lengths.

2.4.1. Uncoupled interface

Accounting for the total, effective frictional flux Q that is applied simultaneously to nodes w2 and t1, the uncoupled system is modeled by the following combination of Equations (18) and (19):

$$\begin{pmatrix} w_{11} & w_{12} & 0 & 0 \\ w_{21} & w_{22} & 0 & 0 \\ 0 & 0 & t_{11} & t_{12} \\ 0 & 0 & t_{21} & t_{22} \end{pmatrix} \begin{pmatrix} \theta_{w1} \\ \theta_{w2} \\ \theta_{t1} \\ \theta_{t2} \end{pmatrix} = \begin{pmatrix} Q_{w1} \\ Q_{w2} \\ Q_{t1} \\ Q_{t2} \end{pmatrix} = \begin{pmatrix} Q_{w1} \\ \beta Q \\ (1-\beta)Q \\ Q_{t2} \end{pmatrix}. \tag{22}$$

Here, β is the fraction of heat that is partitioned to the work. Being undetermined, β is commonly set to 0.5 to give equal heat partitioning to the work and tool. This is equivalent to applying the two conditions

$$Q_{w2} + Q_{t1} = \text{constant } Q, \tag{23}$$

$$Q_{w2} - Q_{t1} = 0. \tag{24}$$

2.4.2. Temperature continuity

The algorithm used here for implementing the temperature-continuity condition follows directly that of Tay et al. [1974]. Under temperature continuity,

$$\theta_{w2} = \theta_{t1} = \theta, \tag{25}$$

while at the same time, the total amount of applied, frictional flux is

$$Q_{w2} + Q_{t1} = \text{constant } Q. \tag{26}$$

Equations (25) and (26) represent a redundancy in Equation (22) (first equality) that can be collapsed:

$$\begin{pmatrix} w_{11} & w_{12} & 0 \\ w_{21} & w_{22}+t_{11} & t_{12} \\ 0 & t_{21} & t_{22} \end{pmatrix} \begin{pmatrix} \theta_{w1} \\ \theta \\ \theta_{t2} \end{pmatrix} = \begin{pmatrix} Q_{w1} \\ Q \\ Q_{t2} \end{pmatrix}. \tag{27}$$

Hence, the application of temperature continuity to a coincident, contact-node pair reduces the size of the uncoupled system by one [Tay et al., 1974]. In the 2D algorithm used in this paper, the contact nodes on the work and tool boundaries coincide in location to ease the matrix-reduction procedure.

The far-field boundary conditions

$$\theta_{w1} = \theta_{t2} = 0, \tag{28}$$

are applied to Equation (27). Solving for $\theta = \theta_{w2}$ and re-expanding to Equation (22), the heat partitioned to the work element is found to be

$$\beta = \frac{w_{22} \cdot \theta_{w2}}{Q} = \frac{[(k_{work}/L_{work}) + (\rho_{work}\hat{c}_{work}v/2)]}{[(k_{work}/L_{work}) + (\rho_{work}\hat{c}_{work}v/2)] + (k_{tool}/L_{tool})}. \tag{29}$$

2.4.3. Convective cooling (and flux continuity)

Convection-cooling conditions are formulated using the heat transfer coefficient h and the fraction β of heat partitioned to the work as follows:

$$k_{work}\left.\frac{\partial \theta_{work}}{\partial x}\right|_{x=x_{w2}} = h(\theta_{t1} - \theta_{w2}) + \beta Q, \tag{30}$$

$$k_{tool}\left(-\frac{\partial \theta_{tool}}{\partial x}\right)_{x=x_{t1}} = h(\theta_{w2} - \theta_{t1}) + (1-\beta)Q, \tag{31}$$

Their finite-element weak forms of which are as follows:

$$Q_{w2} = h \cdot (\theta_{t1} - \theta_{w2}) + \beta Q, \tag{32}$$

$$Q_{t1} = \mathrm{h} \cdot (\theta_{w2} - \theta_{t1}) + (1-\beta)Q \tag{33}$$

Substituting Equations (32) and (33) into the first equality of Equation (22) gives:

$$\begin{pmatrix} w_{11} & w_{12} & 0 & 0 \\ w_{21} & (w_{22}+\mathrm{h}) & -\mathrm{h} & 0 \\ 0 & -\mathrm{h} & (t_{11}+\mathrm{h}) & t_{12} \\ 0 & 0 & t_{21} & t_{22} \end{pmatrix} \begin{pmatrix} \theta_{w1} \\ \theta_{w2} \\ \theta_{t1} \\ \theta_{t2} \end{pmatrix} = \begin{pmatrix} Q_{w1} \\ \beta Q \\ (1-\beta)Q \\ Q_{t2} \end{pmatrix}. \tag{34}$$

Referring to Equation (13), the effective coupling-flux matrix in this case is

$$(F_{ij}) = -\begin{pmatrix} 0 & 0 & 0 & 0 \\ 0 & \mathrm{h} & -\mathrm{h} & 0 \\ 0 & -\mathrm{h} & \mathrm{h} & 0 \\ 0 & 0 & 0 & 0 \end{pmatrix}. \tag{35}$$

Flux continuity is convective cooling with $Q = 0$, which leads to a trivial solution if the system boundary is held at ambient, unless a heat source is specified away from the interface. By comparing Equations (22) and (34), it is seen that flux conditions do not reduce the size of the uncoupled system, but rather alters the "stiffness" matrix. The heat partition β becomes a parameter that can be varied.

2.4.4. Mixed interfacial behavior

In the 2D implementation of interfacial coupling, the presence of many interface node pairs requires consistent book-keeping. The added complication, however, allows us to consider inhomogeneous interface behavior.

2.5. Simulation results

Figure 7 illustrates the refined mesh used for the numerical solution. For imposing coupling conditions, node pairs across the tool-chip interface coincide in

location at each step of mesh refinement. A separate refinement near the end of the tool-chip contact helps to resolve the temperature jumps for loose-contact conditions. Table 3 summarizes the parameters used in the simulation.

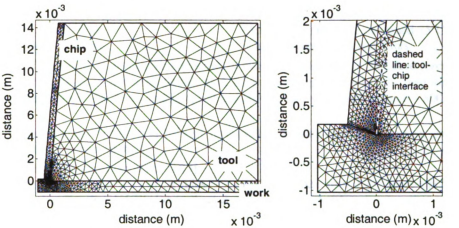

Figure 7. Mesh used for 0-th order problem, and a magnified view

Table 3. Parameters used in the 0th-order problem (background temperature)

Work piece†: AISI 1045 work piece	Tool†: Kennametal TPG322, K-11 Co-cemented
Thermal conductivity†† k_{work} : 50.8 N/(s °C)	Thermal conductivity‡ k_{tool} : 84 N/(s °C)
Density ρ_{work} : 7870 kg/m^3	Specific heat capacity‡‡ $\rho_{tool} \cdot \hat{c}_{v,\,tool}$: 3e6 J/(m^3 °C)
Specific heat†† $\hat{c}_{v,\,work}$ = 486 J/(kg °C)	
Uncut-chip thickness†: 173μm	Rake angle†: 5 degrees
Cut-chip thickness: 519μm	Ambient temperature: assumed 25°C
Out-of-plane width†: 2 mm	Cutting speeds†: 2.5 and 4 m/s

Calibrated cutting forces,††† uncoated carbide tool, 4 m/s: cutting force ≈ 1170N, feed force ≈ 494N.
Calibrated cutting forces,††† uncoated carbide tool, 2.5 m/s: cutting force ≈ 1222N, feed force ≈ 516N.
(Cutting forces reported† for 4 m/s cutting speed and HfN-coated tool: cutting force ≈ 800N, feed force ≈ 330N)

Interface contact lengths‡‡‡: from 0 to 1.2 mm, intimate/temperature-continuity contact; from 1.2 to 1.8 mm, loose/convective-flux contact.

† taken from [Subramanian et al., 1993]

‡ information on conductivity of carbides is scant; data is taken from *CRC Materials Science and Engineering Handbook*, CRC Press, Boca Raton, FL, 2001, p. 405

†† taken from *Properties and Selection: Irons, Steels, and High-Performance Alloys*, Metals Handbook, Tenth Ed., Vol. 1, ASM International, Materials Park, OH, 1990, pp. 197-198

‡‡ approximated from Tlusty, *Manufacturing Processes and Equipment*, Prentice Hall, Upper Saddle River, NJ, 2000, p. 435

††† forces calibrated from HfN-coated-tool data to obtain the same average interface temperature reported by Subramanian et al. for uncoated tools (1250°C for 4 m/s; 1100°C for 2.5 m/s)

‡‡‡ Contact length is reported in Subramanian et al. for the uncoated carbide tool only for the case of cutting at 4 m/s. From Figure 7 of Subramanian et al. [1993, p. 296], the contact length increases approximately linearly from 0.8mm to 1.6mm, corresponding to 3 to 30 seconds of cutting. Since the tool-chip interface temperature for 240 m/min stabilized after approximately 15 seconds, we assume a steady state contact length of 1.2 mm, or 1200 microns. The development of contact length up until the final value of approximately 1800 microns is also taken from Subramanian et al. Because our main interest is in illustrating mass transfer, the same contact length is used for the case of 150 m/min for simplicity.

For simplicity, the only coupling between the tool and the chip is through the tool-chip contact (i.e., the flank wear-land is assuming to be zero and conditions are adiabatic there).

2.5.1. Mixed interfacial behavior

Two-thirds of the tool-chip contact interface, from 0 to 1.2 mm, is prescribed by temperature-continuity conditions. The remaining, downstream one-third of the interface is convectively cooled with a heat transfer coefficient of h = 1e3 W/(m^2 ·°C).

Figures 8-9 plot comparisons of the heat-partition fields and the corresponding interfacial temperatures. In Figures 8, the heat-partition fields used are compared against what they would have been had temperature continuity been imposed on the entire tool-chip interface:

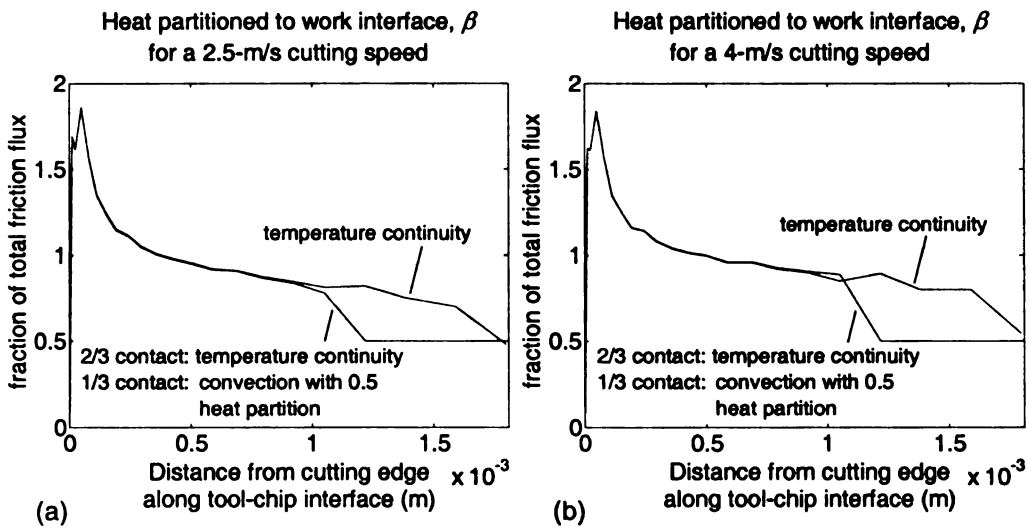

Figures 8a, b. Comparisons of heat partitions of mixed interfacial conditions to the case of pure temperature continuity

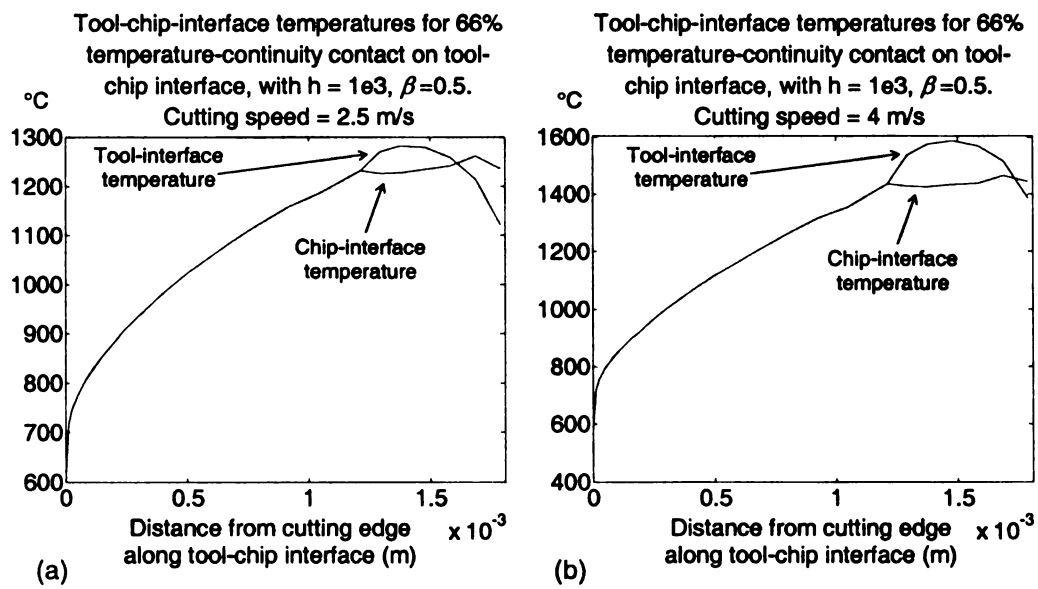

Figures 9a, b. Interface temperatures corresponding to Figures 8

Figures 9 illustrate how the chip-interface temperatures overtake the tool interface temperatures near the end of the tool-chip interface, where the heat partition for mixed conditions overtakes the heat partition for temperature continuity.[5] The size of the temperature jumps also correlates with the differences in the heat partition fields. The location of the crossover point in each set of data, however, is not easy to predict.

2.5.2. Temperature fields

Finally, Figures 10a, b plot the full solution to the 0-th order problem corresponding to the two cutting speeds.

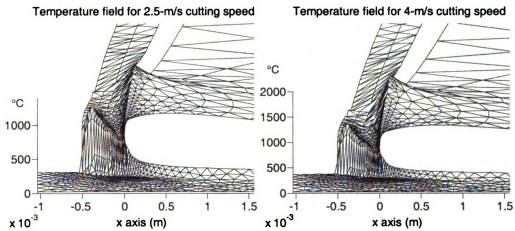

Figures 10a, b. Temperature fields (see also Figures 9a, b)

The extremely rapid rise of the temperature field across the primary shear zone, and a less rapid but still substantial rise adjacent to the tool-chip interface, both contribute to the need for mesh refinement.

[5] The crossover near 1 mm in Figure 8b is considered an imperfect attempt of the numerical scheme to satisfy temperature continuity from 0-1.2 mm and to shift to convective conditions. The main crossover points of interest are associated with the constant heat partition of 0.5, as this is the cause of the difference between Figures 8a and 8b.

Considering that in the case of mixed boundary conditions, the numerical scheme receives no error feedback in its attempt to satisfy temperature continuity, the match in Figures 8 over portions of temperature continuity is very good.

2.6. Summary of the temperature problem

The nature of heat transfer across the tool-chip interface has been studied for the uncoupled interface, the temperature-continuity interface, and the convectively cooled interface. It has been found that the nature of interfacial temperature jumps in all cases except temperature continuity is directly related to the interfacial heat partition. Further, if the work's heat partition is higher (lower) than the value that it assumes in the case of temperature continuity, then the work's interfacial temperature is also higher (lower) than the tool's interfacial temperature, although the crossover points in the two cases are different in general. Namely, the presence of crossovers on the β plots (e.g., Figures 8) correlates with the presence of crossovers in the interface-temperature fields (e.g., Figures 9).

Hence, interfacial temperature jumps are directly related to the heat-partition function in the 1D case (see Appendix), and can be numerically correlated to the behavior of the heat-partition function in the 2D case. The missing link to the actual nature of contact would be a relationship between the heat-partition function and the mechanical nature of frictional contact, but this is beyond the reach of the present work. In the next chapter, the interfacial temperature jumps found in this chapter are assumed, and their effects on dissolution wear will be studied.

Chapter 3

THE FIRST-ORDER PROBLEM OF SPECIES TRANSFER

To completely define the first-order problem, it is necessary to specify the species number N and how mass is exchanged. It is proposed here that the equations of the Frank-Turnbull mechanism be used. The Frank-Turnbull mechanism describes the combination of an interstitial-A atom and a B-lattice vacancy to form a substitutional-A impurity, or

$$A_i + B_V \rightarrow A_s . \tag{36}$$

This reaction is illustrated in Figure 11:

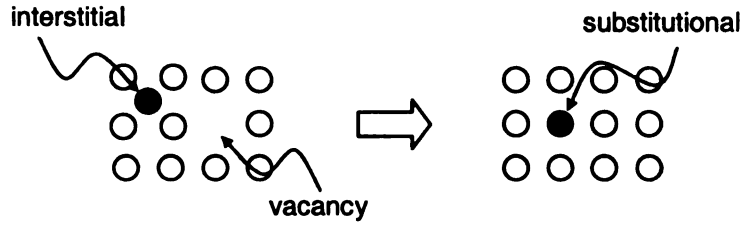

Figure 11: Schematic of the Frank-Turnbull reaction

3.1. The time-dependent equations of the Frank-Turnbull reaction and mass transfer

The governing equations are written using Equations (o) and (p) of Table 2 (with k = 'i', 'V', and 's') for the Reaction (36), where references to A impurity atoms and the B lattice are understood, and all terms are defined in the "Key to Variables, Parameters, and Operators" on page ix:

$$\frac{\partial X_{\mathrm{i}}}{\partial t} = \nabla \cdot \left(D_{\mathrm{i}} \nabla X_{\mathrm{i}} \right) - \nabla X_{\mathrm{i}} \cdot \mathbf{v}^* - \frac{F_{\mathrm{s}}}{c} \tag{37}$$

$$\frac{\partial X_{\mathrm{V}}}{\partial t} = \nabla \cdot \left(D_{\mathrm{V}} \nabla X_{\mathrm{V}} \right) - \nabla X_{\mathrm{V}} \cdot \mathbf{v}^* - \frac{F_{\mathrm{s}}}{c} + \frac{F_{\mathrm{V,psz}}}{c} \tag{38}$$

$$\frac{\partial X_{\mathrm{s}}}{\partial t} = -\nabla X_{\mathrm{s}} \cdot \mathbf{v}^* + \frac{F_{\mathrm{s}}}{c} \tag{39}$$

$$\frac{F_{\mathrm{s}}}{c} = k_{\mathrm{fwd}} \left(X_{\mathrm{i}} X_{\mathrm{V}} - \frac{X_{\mathrm{i,eq}} X_{\mathrm{V,eq}}}{X_{\mathrm{s,eq}}} X_{\mathrm{s}} \right) \tag{40}$$

where F_{s} / c embodies the rate of production of substitutional impurities via the Frank-Turnbull reaction [Sturge, 1959; Giese et al., 2000]. The term $F_{\mathrm{V,psz}} / c$ is defined by

$$\frac{F_{\mathrm{V,psz}}}{c} = k_{\mathrm{V}} \left(X_{\mathrm{V,eq}} - X_{\mathrm{V}} \right) \tag{41}$$

and represents the generation of vacancies within the primary shear zone only (see Figure 3). The impurity subscripts 'i' and 's' can refer to either tungsten or cobalt. In effect, each diffusing tool element is modeled separately as a dilute tracer component. Additional assumptions are the constancy of concentration c, the diluteness approximation ($|F_k| \gg \left| X_k \sum_m F_m \right| = \left| X_k \left(-F_{\mathrm{s}} + F_{\mathrm{V,psz}} \right) \right|$), and the neglect of the diffusive mobility of substitutionals as compared to the mobility of interstitials and vacancies ($D_{\mathrm{s}} \ll D_{\mathrm{i}}, D_{\mathrm{V}}$).

Note that no equation is written for the chip species (iron) in its role as the substrate lattice; however, its presence implies the approximate constancy of the total concentration c, which is an important simplification. Solubility data from binary phase

diagrams are also reported relative to the chip species. Lastly, the concentration-averaged velocity **v*** is approximated to be that of the chip advection velocity.

3.1.1. Boundary conditions for mass transfer

The decomposed tool components are postulated to enter the chip lattice as interstitial impurities. Then, dissolution is controlled by the flux of interstitials entering the chip boundary (viz., the crossing of the bold line from tool to chip in Figure 3):

$$D_{\mathrm{i}} \frac{\partial X_{\mathrm{i}}}{\partial n} = l_{\mathrm{diss}} k_{\mathrm{diss}} \left(X_{\mathrm{i,\,eq}} - X_{\mathrm{i}} \right), \tag{42}$$

where n is the outward normal distance from the tool interface into the depth of the chip, l_{diss} is a length that is used to render a volumetric rate into an area flux, and k_{diss} is the rate constant for the dissolution of tool material into chip, defined by

$$k_{\mathrm{diss}} = A_0 \nu_{\mathrm{Fe}} \exp\left(-\frac{\Delta \overline{g}_{\mathrm{decomp}}}{R\theta} \right) \exp\left(-\frac{\Delta \overline{g}_{\mathrm{activn}}}{R\theta} \right). \tag{43}$$

Here, A_0 is a calibration constant. According to Shewmon [1989, p. 70, pp. 74-75], given the diluteness assumption, $\exp\left(-\Delta \overline{g}_{\mathrm{decomp}} / (R\theta)\right)$ can be interpreted as the mole fraction of decomposed tool components under chemical equilibrium (i.e., the equality of Condition (v) in Table 2), and $\nu_{\mathrm{Fe}} \exp\left(-\Delta \overline{g}_{\mathrm{activn}} / (R\theta)\right)$ can be interpreted as the jump frequency of tool constituents moving into the work lattice under chemical equilibrium.[6]

---

[6] The interpretation makes use of the idea of activated complexes (i.e., vibration-activated openings on the chip surface through which tool constituents pass). In an earlier edition of his book, Shewmon [1963, p. 60] notes that the "precise definition of v is one of the more difficult aspects of a rigorous theory. However, it is usually taken equal to the Debye frequency." Shewmon [*ibid.*, p. 60] continues to say that the entire derivation hinges on the assumption that $\Delta \overline{g}_{\mathrm{activn}}$ "is a state function, that is, that the free energy of the activated complex attained by the reversible process is the same as the free energy of the

In this interpretation, we can also view the interstitial boundary flux $D_i \partial X_i / \partial n$ as the product of the concentration of open sites for interstitials, times the product of the probabilities (i.e., mole fractions) of decomposition and activation, times the frequency that the tool constituents are allowed to jump into a lattice site within the chip. Hence, we define dissolution wear as the combined sequence of events of decomposition at the interface and the subsequent advection-diffusion-reaction within the chip region.

X_V and X_S are simply given zero mass flux boundary conditions; the validity of this choice for the advection boundaries is discussed in [Zienkiewicz and Taylor, 2000b, pp. 44-46]. The same condition applies for X_i along all parts of the boundary except the tool-chip interface.

3.2. Connection to previous work by Kramer

The role of the rate constant is to determine the rate of rise of the interstitial distributions but not its saturation value $X_{i,eq}$. In fact, simulation results using Equation (42) shows that the solubility $X_{i,eq}$ is the maximum value of X_i that is achievable along the contact interface (Section 3.5.3). This is consistent with the earlier works of Kramer. In particular, mass transfer at the contact interface is rate-controlled by the supply of interstitials, and the solubility $X_{i,eq}$ governs the maximum amount of

---

activated complex that really occurs in nature. This would be true if the complex, like a vacancy, existed for a period long enough to let the surrounding lattice completely adjust to the presence of the complex.... but if the system is not in thermal equilibrium (*present author's note*: i.e., chemical equilibrium), the entire procedure may become only an approximation of doubtful value.... One of the main justifications of this analysis is that it works. It is not clear to many authors just how the assumption discussed above can be fulfilled, but whenever the predictions of this theory have been experimentally checked, the theory has been vindicated."

dissolution wear. At high temperatures, the value of the impurity distribution at the interface approaches its solubility value, and the dissolution effect approaches its peak.

3.3. The time-independent equations

To model time-independent behavior, we set both $\partial(\cdot)/\partial t = 0$ and $F_s = 0$ in Equations (37)-(40). It is implicitly assumed that the chronological order of occurrence of (i) the achievement of a macroscopic steady state, and (ii) the local saturation of the Frank-Turnbull reaction, is immaterial. Under these conditions, X_s can be eliminated by recasting the equations as follows:

$$0 = \frac{\partial X_i}{\partial t} + \frac{\partial X_s}{\partial t} = \nabla \cdot (D_i \nabla X_i) - \nabla (X_i + X_s) \cdot \mathbf{v}^* \tag{44}$$

$$0 = \frac{\partial X_V}{\partial t} + \frac{\partial X_s}{\partial t} = \nabla \cdot (D_V \nabla X_V) - \nabla (X_V + X_s) \cdot \mathbf{v}^* + \frac{F_{V,psz}}{c} \tag{45}$$

$$\text{where } X_s = K_{eq} X_i X_V = \frac{X_{s,eq}}{X_{i,eq} X_{V,eq}} X_i X_V \tag{46}$$

and $K_{eq} = X_{s,eq} / (X_{i,eq} X_{V,eq})$ is the equilibrium constant. Equations of the type (44) and (45) have been referred to by Sturge [1959, p. 298] as the equations of atom conservation and lattice-site conservation.

3.4. The difference between W and Co profiles; non-dissolution mechanisms

The difference in W and Co concentrations in Figure 1 is not likely due to electrical mechanisms. WC-Co is metallically bonded, and when it is dissolved into Fe, the components W and Co are most likely charge-neutral interstitials.

Comparisons of atomic radii and decomposition energies do not account for the difference in the W and Co profiles, either. Since Co and W have similar atomic radii as iron, the activation energy required for Co and W to enter the chip lattice ($\Delta\overline{g}_{\text{activn}}$) should be similar. In addition, the free energies of decomposition entering the calculations for W and Co are one and the same (viz., $\Delta\overline{g}_{\text{decomp}}$ of WC $\rightarrow$ W + C).

Referring to the impurity-flux condition, Equation (42), the only remaining factor for explaining the difference between W and Co profiles is the solubility $X_{\text{i, eq}}$. While the solubility of Co in Fe is much higher than the solubility of W in Fe [Hansen et al., 1958, p. 472], the actual amount of Co dissolved in the chip is capped by the supply of decomposed tool material, and hence should be in the same molar proportion to W as found in the tool. To check the W-Co ratios before and after cutting, the data of Subramanian et al [1993] is converted into molar bases in Figures 12a, b:

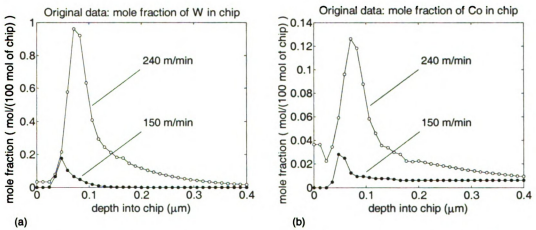

Figures 12a, b. Experimental concentration profiles, deduced from Subramanian et al. [1993]. Empty and filled circles denote data points. In (b), the 240-m/min curve asymptotes to the same non-zero value as the 150-m/min curve.

Incidentally, the maxima and minima of the concentration profiles for the W and Co for a given speed occur at the same depths, which shows that Co has similar mobility as W as both constituents move through the chip lattice. We now check the molar ratio of W and Co within the chip and compare it to the corresponding molar ratio within the fresh tool material. The areas under both the W and the Co profiles are assumed to be representative of the total moles per unit length in the chip flow direction. For the case of 240-m/min cutting speed, we find that the W-to-Co ratio of absorbed moles per unit length (i.e., the ratio of the W and Co areas for the case of 240-m/min cutting speed) is 5.34-to-1. On the other hand, it turns out that the molar/atomic composition of the tool is 45.6% W, 45.6% C, and 8.1% Co (with a trace of TaC-NbC), or a W-to-Co ratio of 5.63-to-1. Considering that the 5.34-to-1 ratio is calculated from a single sectioned profile, it is considered a good match to the 5.63-to-1 ratio. Hence, we find consistency with the hypothesis that Co maintains its molar ratio with W before and after cutting. For the case of 150-m/min cutting speed, the same process of calculating the W-to-Co molar ratio per unit length from Figures 12a, b returns a low value of 2. The cause of this low value is the non-vanishing tail in the Co profile after a depth of 0.1μm in Figure 12b. We choose to ignore this tail on the hypothesis that the detected Co traces are related to the W traces in roughly the same molar ratio inherited from the fresh tool, and the fact that the W profiles decay to zero.[7] Using maximum values from the profiles instead, we obtain a W-to-Co molar ratio per unit length of 6.25. This ratio is consistent with an increased amount of interface wear (e.g., abrasion) not accountable by dissolution, and it is

[7] The other interpretation would be that the W profile decays asymptotically to a small, but nonzero value, but this is judged less likely because such a non-vanishing tail with zero flux would require us to introduce a condition of mass buildup at some pre-determined depth. This issue will be revisited later.

explained as follows. Suppose that, for every 100 moles of tool constituents decomposed (i.e., prior to diffusion and advection), 0.96 moles each of W and Co are removed due to various interactions at the interface, and are made inaccessible to diffusion into the chip. Then the W-to-Co molar ratio would change from 45.6-to-8.1 prior to cutting, to (45.6 – 0.96)-to-(8.1 – 0.96) as detected within the chip afterwards, or equivalently, 6.25-to-1. In Section 3.5.4, this calculation is revised to make use of the concentration fields that have been extrapolated from experimental data using the Frank-Turnbull interpretation.

To summarize, our interpretation of the profile data of Subramanian et al. indicates that the W-Co molar ratio found in the chip reflects, in the main, the W-Co molar ratio found the tool. Differences in the W-Co molar ratios before and after cutting can be used to gauge the amount of worn cobalt that is not attributed to dissolution wear. Among non-dissolution-based wear mechanisms are the deposition of tool constituents onto and subsequent advection by the chip (e.g., asperity exchange favored by surface energy changes [Rabinowicz, 1965], 2-body abrasion and deposition through applied pressure, plowing [Suh, 1986], etc), the sweeping action by loose debris in rolling friction (i.e., 3-body abrasion [Rabinowicz et al., 1961; Rabinowicz, 1977]), the deposition of tool constituents onto rolling debris at high pressure—with the number of mechanisms likely limited only by the imagination.

3.5. Results of the species-transfer problem

The interfacial temperature field is gotten from the analysis of Chapter 2, and the result for the 4-m/s cutting speed is reproduced in Figure 13. It is seen that the interfacial

temperatures can vary significantly from its average value. The temperature jump in the region near the end of contact is due to a hypothesized region of loose contact.

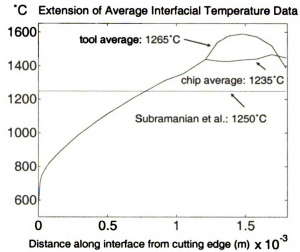

Figure 13. Variation of temperatures away from the average

Figure 14 shows the region of interest and the numerical mesh used for the species-transfer problem:

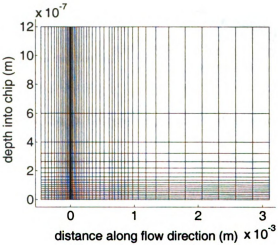

Figure 14. Mesh used in the 1st-order, species-transfer probelm

The x axis from 0 to 1.8 mm corresponds to the tool-chip interface parallel to the flow direction where interstitial impurities are introduced. The y axis corresponds to a very small portion of the primary shear zone where vacancies are generated. The y direction is

the chip-depth direction along which concentration profiles vary, and is plotted on a highly magnified scale. The depth distances are so small that the temperature, and hence the material properties, only vary in the x direction.

A product of interstitials and vacancies leads to the humped concentration profile that is the basis of the present application of the Frank-Turnbull mechanism; for this purpose, a special vacancy distribution is chosen. An example of one such distribution, plotted topographically on the mesh of Figure 14, is shown in Figure 15a:

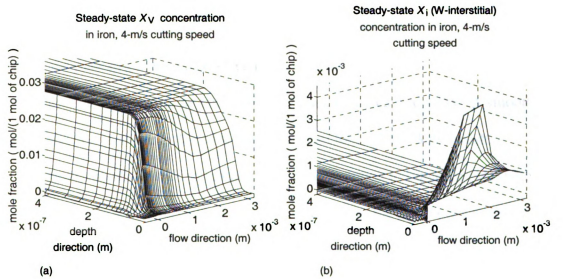

Figures 15a, b. Sample X_V and X_i distributions

The rise of X_V in the depth-direction (y-direction) is obtained empirically by targeting the iterated solutions of the Frank-Turnbull nonlinear equations (Equations (44)-(46)) towards a match with the rise of the profiles found by Subramanian et al., and by retroactively adjusting the input supply of vacancies within the primary shear zone (Equation 7) until the match is within tolerance. The iterated steady-state solution, based on the method of quasi-linearization [Kwon and Bang, 2000, p. 539], is set up so that the

value of X_s after the first iteration is a simple product of X_i and X_V; subsequent iterations account for species transfer.

In Equation (41), k_V is set to be a hyperbolic tangent function of y that is used to introduce a quick rise of vacancies within the primary shear zone, and $X_{V,eq}$ controls the height of the vacancy distribution. The form of vacancy generation in Equation (41) is numerically less demanding than a Dirichlet condition, and it also has the property that as the advection speed increases, the height of the vacancy distribution decreases. The underlying assumption is that the amount of vacancies generated is bounded, and the height of the plateau generated by advection is determined by a competition between the vacancy-generation rate and the rate at which vacancies are carried away. A smooth rise in the x direction is also introduced to avoid the need for a highly dense mesh.

Figure 15b shows the interstitial distribution (solution to Equation (44)) with which the vacancy distribution interacts. For convenience, the parameters governing the boundary condition of the interstitial distribution are collected in Table 4.

Before finishing the discussion on the interstitial distribution which leads to the main results, a digression is taken to explain the two most important parameters, namely, diffusivity and solubility.

Table 4. Parameters used in the 1st-order problem (mass transfer)

Mass flux $D_i \frac{\partial X_i}{\partial n} = l_{diss} \cdot \left(A_0 \nu_{Fe} \exp\left(-\frac{\Delta \bar{g}_{decomp}}{R\theta} \right) \exp\left(-\frac{\Delta \bar{g}_{activn}}{R\theta} \right) \right) \cdot \left(X_{i,eq} - X_i \right)$

A_0 : 1 (assumed; as long as this number is of order 1, the sensitivity of the steady-state results to its variations is low)

l_{diss} : 2.5×10^{-8} m (≈ lattice distance; D. Gaskell, *Introduction to Metallurgical Thermodynamics*, 2nd ed., Hemisphere Publishing Corporation, 1981, pp. 117-118)

ν_{Fe} : $1 \times 10^{+13}$ s^{-1} (≈ Debye frequency; D. Gaskell, *Introduction to Metallurgical Thermodynamics*, 2nd ed., Hemisphere Publishing Corporation, 1981, p. 118)

$\Delta \bar{g}_{decomp}$: 9000 cal/mol (from the reaction WC→W+C; O. Kubaschewski, E. L. Evans, and C. B. Alcock, *Metallurgical thermochemistry*, 4th edition, Pergamon Press, Oxford, 1967, p. 429. Actually, it is 9000–0.4θ cal/mol, but $\exp(-(9000 - 0.4\theta)/(R\theta))$ becomes $\exp(+0.4) \cdot \exp(-9000/(R\theta))$, and the exp(+0.4) term is grouped into the constant A_0.)

$\Delta \bar{g}_{activn}$: 18000 cal/mol (4-m/s cutting speed); 21000 cal/mol (2.5-m/s cutting speed) (curve-fit value that controls the maximum of X_s (adjusted after α below is determined))

$X_{i,eq} = \alpha X_{W,eq}$ and $X_{s,eq} = (1-\alpha) X_{W,eq}$, where $\alpha = 0.0375$ (4-m/s cutting speed), and $\alpha = 0.0150$ (2.5-m/s cutting speed) (α is the first curve-fit value determined)

$X_{W,eq} = 9 \times 10^{-11} T_C^3 - 1.23 \times 10^{-7} T_C^2 + 7.6 \times 10^{-5} T_C - 9.8 \times 10^{-3}$, where T_C is temperature in Celsius. (Value of $X_{W,eq}$ taken from solubility curve of W-Fe binary phase diagram, p. 734 of *Constitution of Binary Alloys*, 2nd edition. Metallurgy and Metallurgical Engineering Series, McGraw-Hill, New York, 1958. Cubic best fit from Microsoft Excel)

$X_{Co,eq} = \varphi X_{W,eq}$: $\varphi = 0.125$ (4-m/s cutting speed); $\varphi = 0.185$ (2.5-m/s cutting speed) (§3.5.4)

Remaining parameters:

$X_{V,eq}$ = 0.035 (curve-fit value that affects the rise of X_s through its influence on X_V 's rise)

D_i : $1 \times 10^{-10.925}$ m^2/s (4 m/s-cutting speed); $1 \times 10^{-11.725}$ m^2/s (2.5-m/s cutting speed) (curve-fit value that controls the spread of X_s (adjusted after α has been determined))

D_V : 1×10^{-14} m^2/s (curve-fit value that prevents X_V from losing its shape due to advection)

D_s : neglected in this analysis

k_V : quick rise to a value of 0.25 (curve-fit function that controls the rise of X_V, and hence X_s, within the primary shear zone)

k_{fwd} : $1 \times 10^{+5}$ s^{-1} (curve-fit value that controls the Frank-Turnbull reaction rate during relaxation)

p_0 : $0.3 \times 10^{+9}$ N/m^2 (force/contact area; needed for studying effect on diffusivities, both in decreases in magnitude and variations across the ferrite-austenite transition temperature)

3.5.1. Unusually low values of mass diffusivities

Figures 16a, b show a comparison of the tungsten-interstitial diffusivity $D_{W\text{-in-}Fe}$ and iron-vacancy diffusivity D_V used in the simulations versus those found from tables[8]:

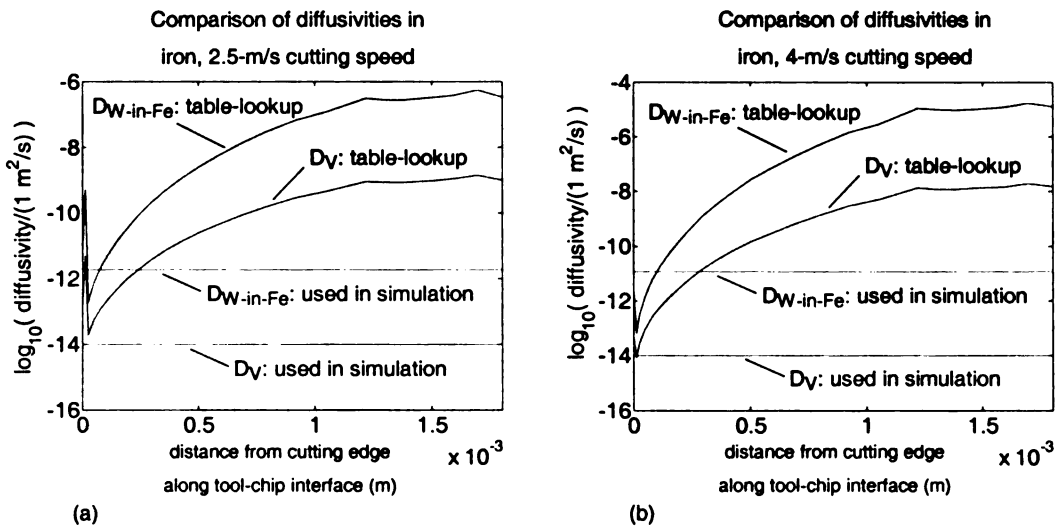

Figures 16a, b. A comparison of available values of diffusivities versus actual values used in simlations for (a) 2.5-m/s cutting speed, (b) 4-m/s cutting speed

A small D_V prevents the vacancy distribution from losing its shape downstream of the primary shear zone, which is needed to model the quick rise (within a 0.1-μm distance) of the concentration profile of Subramanian et al. [1993] (Figures 1 and 12 in this work). Also, D_i must be small enough to force a quick decay (also within a distance of 0.1 μm). Values of diffusivities available in the literature are simply too large to achieve these

[8] Spatial dependence of mass diffusivity is due to the background temperature and pressure fields from the 0th-order problem. The sharp drops in mass diffusivities near the origin correspond to the ferrite-to-austenite transition point, which, at a pressure of 0.33e9 Pa, is approximately 718°C. Table-lookup values are taken from Elliot et al. [1963] as Arrhenius functions of the absolute temperature. Constant values of mass diffusivities are adopted in the simulation for a practical reason: a sharp drop in diffusivity requires mesh refinement for resolution and numerical stability, especially in the presence of strong advection. Physically, however, most tool wear occurs downstream of the cutting edge (e.g., the boundary values of interstitials in Figure 15b) where the mass diffusivity is almost constant, hence the use of constants.

As mentioned in Section 3.4 (discussion of Figures 12), the diffusivity of Co is rate-limited to that of W.

effects. In fact, the use of the table-lookup diffusivities leads to vacancy and interstitial distributions that are shown Figures 17a, b:

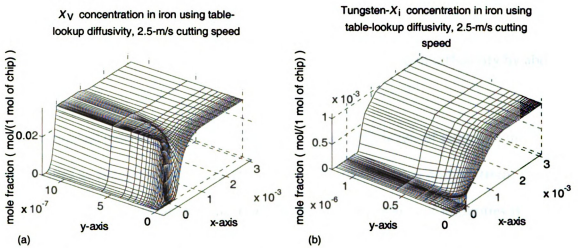

Figures 17a, b. X_V and X_i distributions using table-lookup values of Figures 16

In contrast to the distributions of Figures 15, neither a rapid-rise function nor a decaying function is present, and the product of the distributions in Figures 17a, b will not result in a humped distribution in the *y*-direction as required.

Pressure and damage are two possible reasons for the seeming prevalence of low values of diffusivities. Although pressure does not enter explicitly in the equilibrium condition (equality of Condition (v) in Table 2), it tends to decrease the values of diffusivities. An expression by Shewmon [1989, pp. 84-85] illustrates this relationship:

$$\left[\frac{\partial}{\partial p_0}\ln\left(\frac{D}{l_{\text{diss}}^2 \nu_{\text{Fe}}}\right)\right]_{\theta \text{ fixed}} = -\frac{\overline{V}_{\text{activation}}}{R\theta}, \tag{47}$$

where $\overline{V}_{\text{activation}}$ is the activation volume (in m^3/mol), and it is known to be smaller than the molar volume of the lattice metal (viz., iron). Assuming constancy of all terms except *D* for simplicity, we have that

$$\frac{D(p_0)}{D(1\ \text{atmosphere})} = \exp\left(-\frac{p_0 \bar{V}_{\text{activation}}}{R\theta}\right). \tag{48}$$

For a pressure of p_0 of $0.33\times10^9\ \text{N/m}^2$ at 1000K and a maximum $\bar{V}_{\text{activation}}$ value of $M_{Fe} \div \rho_{Fe} \approx 7\times10^{-6}\ \text{m}^3/\text{mol}$, we arrive at a maximum drop in diffusivity by about a factor of 3.

Damage mechanisms may be needed to achieve the levels of reduction in diffusivities as suggested by Figure 16. That is, the concentration profiles from experiments may reflect shear damage so severe that the mobility of impurities is significantly impaired. However, no simple, independent test of this hypothesis is available at this time, and the mass diffusivities are considered curve-fit parameters.

3.5.2. The determination of interstitial solubility; post-machining relaxation

In an early development of the model for tungsten impurities, $X_{i,eq}$ and $X_{s,eq}$ are *both* set equal to $X_{W,eq}$ because the fractions of interstitials and substitutionals among a given amount of impurities are unknown. Figure 18 shows the result of a simulation for the steady-state, substitutional distribution under the assumption $X_{i,eq} = X_{W,eq} = X_{s,eq}$ for the 2.5-m/s cutting speed. The section taken—where comparison is made with the profile from the data of Subramanian et al.—corresponds to the chosen distance of x = 1.8 mm; this is the end of the tool-chip contact where impurity concentrations are near or at their maximum for a variety of loading conditions.

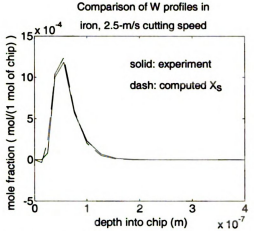

Figure 18. Good match in an early run that turns out wrong

Despite a good match, it is remembered that the measured concentration also includes the residual interstitial distribution at the end of cutting (i.e. steady state). The residual X_i field is given as a topographical plot in Figure 19a, and its sectioned profile is superposed onto Figure 18 and presented in Figure 19b:

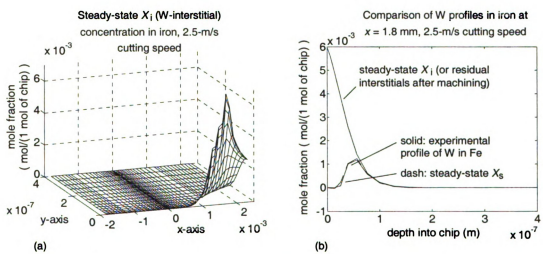

Figures 19a, b. Why the good match of Figure 18 does not work

The sum of the steady-state X_s and X_i distributions no longer agrees with data.

Evidently, $X_{i,eq}$, which controls the maximum of X_i along the tool-chip interface, must be decreased, as reflected by the multiplicative factor α in Table 4. In

fact, the value of α from the curve fit represents the fraction of impurities that can be identified as interstitial impurities, as seen from the following equations:

$$X_{\mathrm{i,eq}} = \alpha X_{\mathrm{W,eq}} \text{ and } X_{\mathrm{s,eq}} = (1-\alpha)X_{\mathrm{W,eq}} \tag{49}$$

Figure 20a show that decreasing $X_{\mathrm{i,eq}}$ forces the steady-state X_{s} distribution to decay too rapidly. A completely analogous situation occurs for the case of 4 m/s cutting speed:

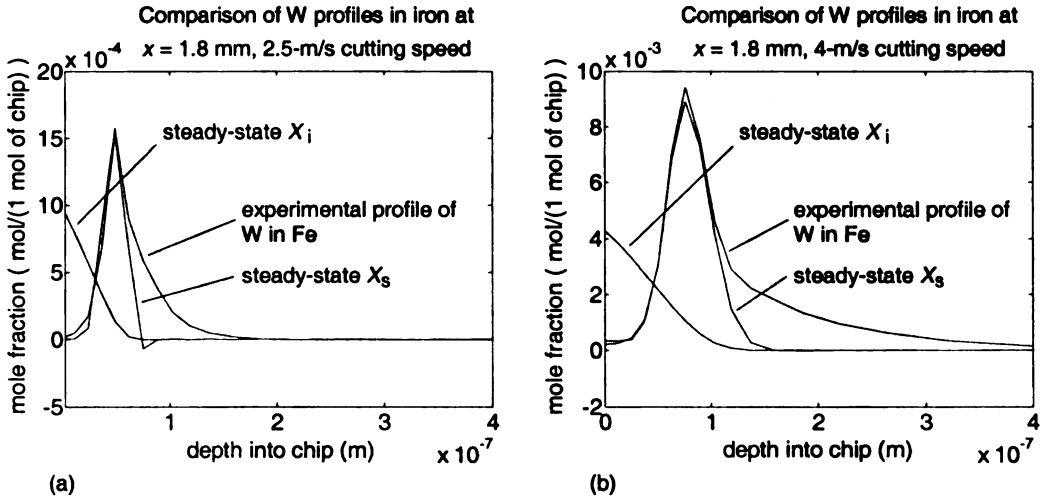

Figures 20a, b. Attempts at matching experimental W-concentration profiles using only steady-state W distributions from the model

Increasing D_{i} delays the decay of X_{s} in Figures 20, but the spread of the distribution is unacceptably increased (not shown in Figures 20) beyond the experimental-data curve.

At this point it is thought that a relaxation process may take place after cutting—but before quenching—such that the tail of the steady profile would 'fill up' to match the experimental curve. To test this hypothesis, we model Equations (37)-(39) with time dependence, zero advection speed, homogeneous flux boundary conditions, and with the X_{i}, X_{V}, X_{s} distributions inherited from the steady-state calculation. Also, the temperature field is preserved as quenching has not yet occurred. The result of such a

relaxation run for the case of 4-m/s cutting speed is shown in Figure 21a. The solid X_s curves correspond to the relaxation times of 0, 0.9, and 3.6 milliseconds; it is found that the peak of X_s rises to a maximum value at approximately 0.6 milliseconds before it decreases thereafter. For a choice of a uniform and steady reaction-rate constant k_{fwd}, the match to experimental data is considered reasonably good.[9] Figure 21b shows the relaxed X_s field at the final time; a practical choice of the coarsest mesh possible leads to wiggles on order of 3% of the maximum value of X_s:

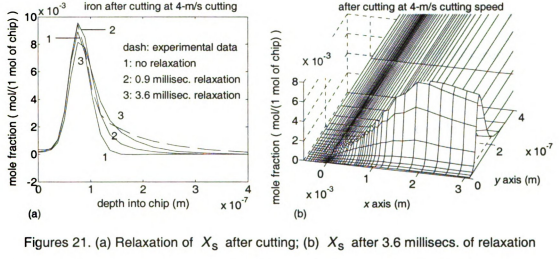

Figures 21. (a) Relaxation of X_s after cutting; (b) X_s after 3.6 millisecs. of relaxation

Figure 22a shows the final outcome of the relaxation simulation (starting from the state of Figure 20b) at 3.6 milliseconds. Figure 22b plots the volume under the X_s plot as a

[9] The use of a non-uniform k_{fwd} can improve match but extra physical mechanisms have to be introduced. The size of k_{fwd} determines the speed of relaxation; for example, the elapse time for the relaxation process to nearly exhaust the tungsten X_i in Figures 19b is roughly 3.6 milliseconds, corresponding to k_{fwd} = 1e5 s^{-1}. The uniformity of k_{fwd} implies uniformity in reaction rates given a uniform driving force; however, because a low value of D_V maintains a vacancy-depletion zone near the interface, there are no renewed, Frank-Turnbull reactions there. Consequently, the rise of the X_s hump is not significantly altered during post-machining relaxation.

The elapsed time after machining but before quenching of the chips is not given in the original data.

function of relaxation time after cutting. It is seen that the residual X_i field is essentially exhausted through its interaction with X_V.

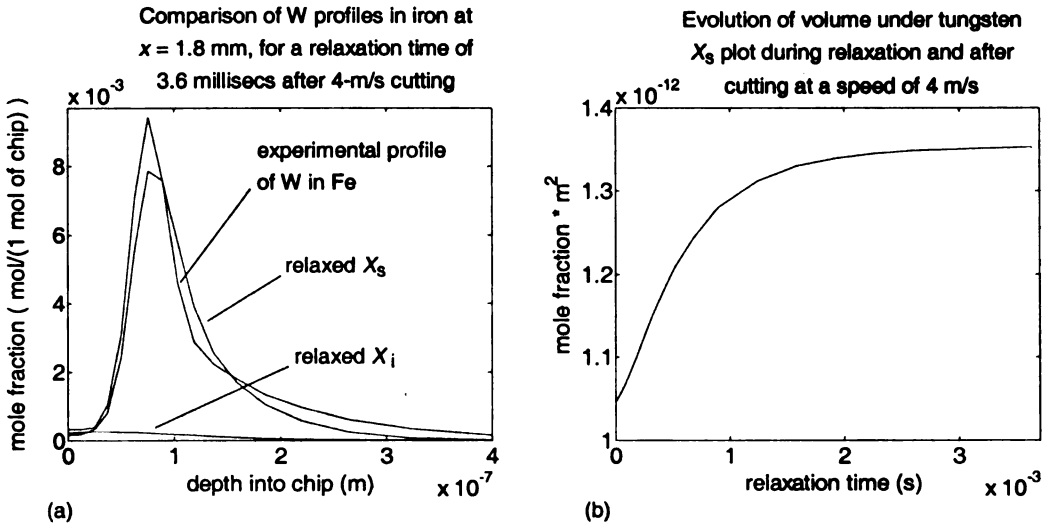

Figures 22a, b. A check on the exhaustion of tungsten X_i during relaxation

3.5.3. Solubility as the maximum amount of dissolution wear achievable

Figures 23a, b show how the equilibrium solubility $X_{i,eq}$ (as defined by Table 4) places bounds on the amount of a tool constituent that is made available for dissolution in the chip.[10] Plots are shown for tungsten; since $X_{i,eq}$ for cobalt is some fraction of $X_{i,eq}$ for tungsten (viz., the product of α and φ as discussed in Sections 3.5.2 and 3.5.4), the plots for cobalt are exactly analogous. If $\Delta\bar{g}_{activn}$ is very large within the expression for the rate constant of dissolution k_{diss} (the second Arrhenius exponential in Equation

[10] The wiggles in X_i near the origin reflects the difficulty with which the coarse mesh tries to resolve a sudden increase. Fortunately, these wiggles do not pose a significant problem in the convergence of numerical solutions, but they do affect accuracy. The tradeoff in mesh coarseness is necessary, as the relaxation runs cost well over 8 hours to run on a computer with a 1.2 GHz processor.

(43)), then the spatial increase of X_i towards its maximum amount is delayed; as $\Delta\bar{g}_{activn}$ increases indefinitely, X_i tends uniformly to zero because the boundary flux does.

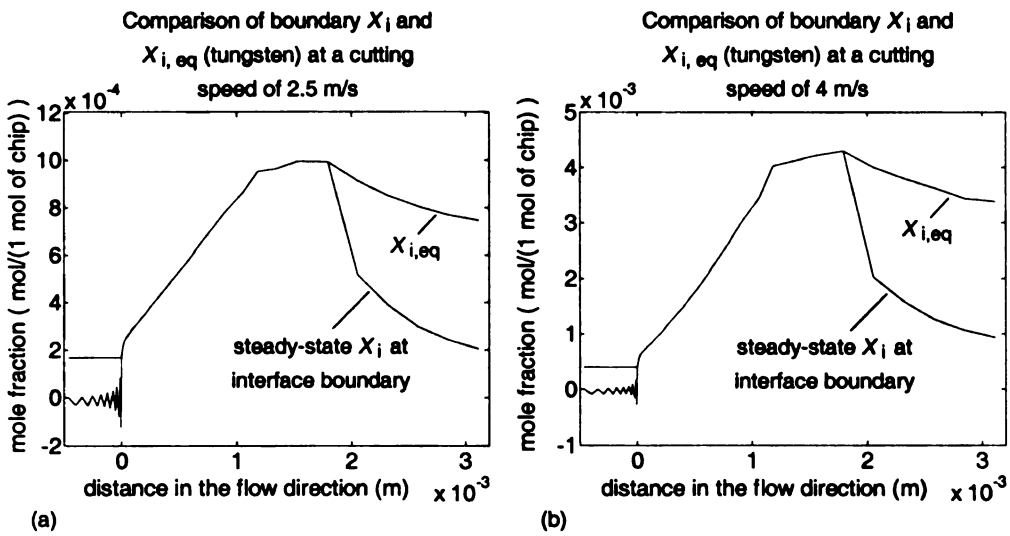

Figures 23a, b. A check of Kramer's hypothesis that dissolution wear is bounded by solubility

It is seen that in going from 2.5 m/s to 4 m/s, the maximum of the boundary supply of interstitials increases by 40 times. While the Arrhenius dependence on temperature of the boundary interstitial flux is influential (Equations (42) and (43)), Figures 23a, b show that solubility is the controlling factor. Further, the sudden change in slope at 1.2 mm reflects the drop in the interfacial temperature of the chip in relation to the tool in the last thirds of contact (see Figure 13).

3.5.4. Amount of worn cobalt not due to dissolution wear

By comparing the molar ratios of W to Co within the chip and within the tool, the amount of worn cobalt not due to dissolution wear can be estimated. Relaxation of the

tungsten profile after cutting at 4 m/s has already been shown in Figure 22b. Figure 24a shows snapshots of the relaxation process for cobalt impurity atoms after cutting at 4 m/s, and Figure 24b is a check on the exhaustion of X_i-cobalt during relaxation:

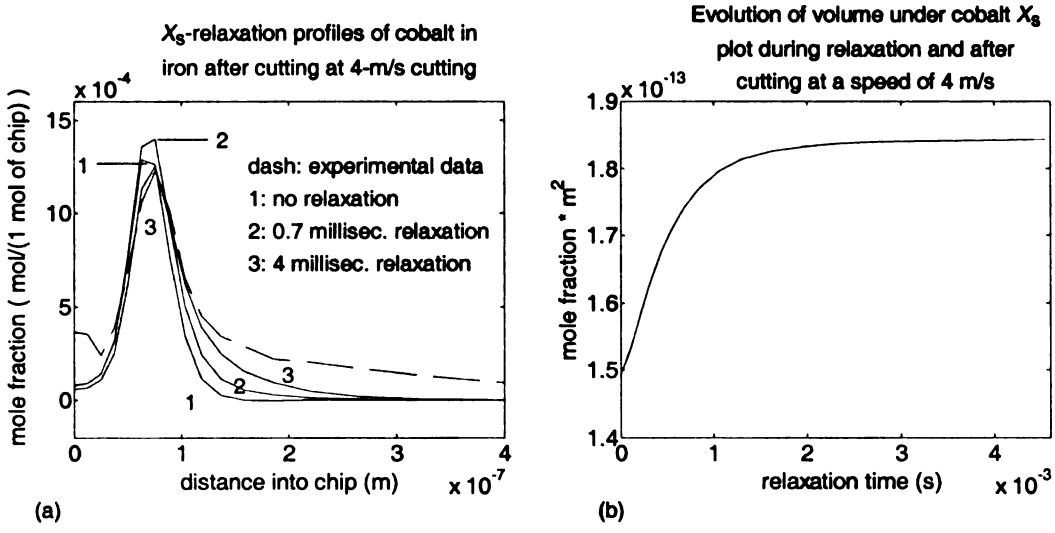

Figures 24a, b. The relaxation process. A check on the exhaustion of cobalt X_i during relaxation

Concentration data suggests that the mobility of Co is similar to the mobility of W as tool constituents diffuse into the chip lattice (Section 3.4). For simplicity, then, the mass diffusivities of Co and W are set equal. The solubility of Co is source-limited to the amount that is originally present in the tool; in particular, the original W-Co molar ratio within the tool is approximately preserved. In the simulations, $X_{\mathrm{Co,\,eq}}$ is set equal to $\varphi X_{\mathrm{W,\,eq}}$, with φ as given in Table 4.[11] Hence, with the exception of φ, all parameters in the W and Co simulations are the same. Given these assumptions, the agreement is deemed reasonable. The thick tail of the experimental curve has been discussed in

[11] That φ has to be empirically determined may be a reflection that not all Co particles enter the chip.

Section 3.4 (Figure 12b and discussion).[12] The initial dip in the experimental data of Figure 24a (dashed curve) may represent residual X_i-cobalt due to quick quenching; however, no independent confirmation is available at this point.

The quotient of the integrated X_s-tungsten evolution in Figure 22b and the integrated X_s-cobalt evolution in Figure 24b is taken to be the evolution of the total W-Co mole fraction within the chip. This W-Co mole-fraction evolution, corresponding to the case of 4-m/s cutting speed, is shown in Figure 25a:

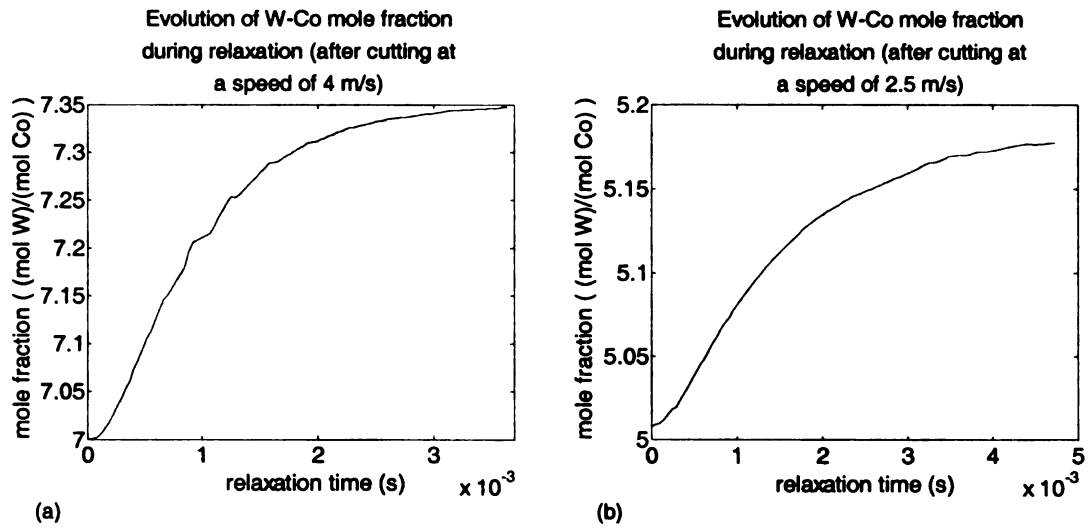

Figures 25a, b. The W-Co ratio within the chip as residual X_i's are exhausted during relaxation for (a) 4-m/s cutting speed, (b) 2.5-m/s cutting speed.

The X_i of both species approaches exhaustion when the amount of X_s stops increasing; hence, we take the final W-Co mole fraction within the chip to be approximately 7.35-to-1 as indicated by Figure 25a. We note that the molar composition of the tool is 45.6% W,

[12] That is, we disregard the thick tail as an artifact because non-zero asymptotes at large depths do not reconcile with the usual picture of exponential decay. If need be, the thick tail can be modeled either by a mass buildup at some depth y, or by changing the way the vacancy distribution increases with depth. The present vacancy distribution saturates to a plateau as seen in Figure 15a.

45.6% C, and 8.1% Co (with a trace of TaC-NbC), or a W-to-Co ratio of 5.63-to-1. To produce a 7.35-to-1 ratio within the chip, we hypothesize that for every 100 moles of tool decomposed, A_W moles of W, A_C moles of C, and A_{Co} moles of Co are lost due to non-dissolution mechanisms; that is, the apparent W-Co molar ratio as seen by the chip is

$$\frac{45.6 - A_W}{8.1 - A_{Co}} = 7.35. \tag{50}$$

A_W, A_C, and A_{Co} are fixed by one extra piece of information from measurements: When the mole fraction of intact WC lost to non-dissolution wear is equated to the residual WC found (the chips are dissolved in hydrochloric acid), it is found to be $(234\mu g/M_0) \div (3517\mu g/M_0) = 0.066$ [Subramanian et al., 1993, Table 1], where M_0 is the molecular weight of WC. Alternatively, the total number of moles of WC lost to non-dissolution wear out of 100 moles is

$$A_W + A_C = 2A_W = 6.6 \text{ moles}. \tag{51}$$

The solution to Equations (50) and (51) is that $A_W = 3.3$ moles and $A_{Co} = 2.345$ moles. Hence, out of every 100 moles of tool material decomposed, about $2A_W + A_{Co} \approx 9$ moles are unavailable to the dissolution mechanism for the 4-m/s experiment. A similar calculation is carried out for the case of 2.5-m/s cutting speed, with '7.35' in Equation (50) replaced by '5.18' (Figure 25b), and with '6.6' in Equation (51) replaced by '33.6' [Subramanian et al., 1993, Table 1]. The corresponding solution is that, out of every 100 moles of tool material decomposed, 16.8 moles of W, 16.8 moles of C, and 2.54 moles of Co are lost to non-dissolution wear at a cutting speed of 2.5 m/s. More sophisticated

models of non-dissolution wear can be used if information is known about the amount of tungsten lost beyond the amount that is lost as intact WC grains.

3.5.5. The rate of tool wear as a field quantity

An analogous relation to Equation (42) can be written to describe the flux of material leaving the tool interface

$$-\left(D_{\mathrm{i}}\frac{\partial X_{\mathrm{i}}}{\partial n_{\mathrm{tool}}}\right)_{\mathrm{tool}} = l_{\mathrm{decomp}}k_{\mathrm{decomp}}\left(X_{\mathrm{i,eq}} - X_{\mathrm{i}}\right), \tag{52}$$

where n_{tool} is the outward normal distance to the tool interface, l_{decomp} is used to render a volumetric rate into an area flux, and k_{decomp} is the rate constant for the decomposition of tool material defined by

$$k_{\mathrm{decomp}} = B_0\nu_{\mathrm{tool}}\exp\left(-\frac{\Delta\bar{g}_{\mathrm{decomp}}}{R\theta_{\mathrm{tool}}}\right) \tag{53}$$

Figure 26a shows a plot of $l_{\mathrm{decomp}}k_{\mathrm{decomp}}$ for $l_{\mathrm{decomp}} \approx 2.5\times10^{-8}\,\mathrm{m}$, $B_0 = 1$, $\nu_{\mathrm{tool}} \approx 1\times10^{13}\,\mathrm{s}^{-1}$ for the case of 4-m/s cutting speed, and Figure 26b shows the corresponding boundary temperature:

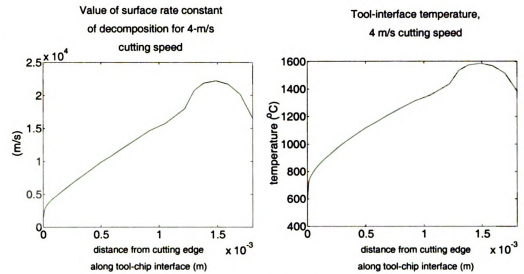

Figures 26a, b. The surface rate constant for tool decomposition and tool-interface temperature

The similarity in functional forms suggests that the contribution to the wear contour is a direct consequence of the interfacial temperature profile, which is recognized early on by Chao and Trigger [1955, p. 1117].

Recently, Molinari and Nouari [2002] have also reported calculations showing that experimental wear profiles on the tool are consistent with the diffusion mechanism. Instead of using a boundary flux condition as reflected by Equation (42) or Equation (52), Molinari and Nouari use Dirichlet-type conditions. While the model of Molinari and Nouari is sufficient to describe the tool-interface contour, the use of a single diffusion equation for the chip region with a Dirichlet boundary condition leads to exponentially decaying profiles of tool components into the chip; this stands in contrast with the findings of Subramanian et al. The question of whether Dirichlet or flux conditions are the proper ones to be applied at the interface may well be decided by details at the interface. However, it is noted that the boundary condition of Equation (42) behaves as a

Dirichlet condition when the dissolution rate constant is high enough to guarantee that the interstitial solubility is reached along the interface (e.g., Section 3.5.3).

3.6. Measurement methods for checking the distribution of vacancies

Macroscopic measurement methods of vacancies such as dilatometry [Paris et al., 1975] measure bulk changes in volume and are not suitable for charting spatial distributions. Evidently, highly sensitive methods operating at the level of microstructures are required. Two such methods for measuring the distribution of vacancies are field ion microscopy and the tracking of positron annihilation (which includes positron lifetime spectroscopy and gamma-ray angular correlation). Although experimental work involving these two methods has yet been applied to the machined chip, a brief description is included here for completeness.

In field ion microscopy, the specimen is sharpened to a submicron-size point and a high voltage is applied to create an electric field at the tip that alternately polarizes and attracts, then ionizes and repels, the atoms of an imaging gas (e.g., neon). The gas molecules are energized according to the protrusions and indentations of the microstructure at the specimen tip, and are propelled in a radial direction towards a phosphor screen to produce an image. The fluorescent image thus created is then a magnified picture (approximately $\times 10^6$) of the intersection of the specimen microstructure with the surface of the needle point. Useful information is extracted through careful comparisons with crystallographic models. Lattice defects such as vacancies (and in general, point, line, and planar defects) are discernible through changes in image brightness and contrast. A mass spectrometer can also be used to identity

impurity atoms. Although powerful, the use of field ion microscopy requires many control experiments to eliminate visual artifacts; a general discussion and a list of references are given in [Miller and Smith, 1989; Miller et al., 1996].

In the positron method, a stream of positrons created from a radioactive source is directed into a solid. Within the bulk of the solid, these positrons are trapped by lattice imperfections. As positrons are annihilated upon contact with electrons, gamma radiation is released, and a map of the traps, and hence the lattice imperfections, is created. Because positrons are point particles, the resolution of this non-intrusive method is extremely high. However, as positrons are not trapped by interstitials, this method is limited to detection of "open-volume defects" such as vacancies [Hautojärvi, 1979; Krause-Rehberg and Leipner, 1999].

3.7. Non-uniqueness of Frank-Turnbull representation

The most important of the parameters for curve fit are α, $\Delta\overline{g}_{\text{activn}}$, and the diffusivities (Sections 3.5.1, 3.5.2, 3.5.3). Of these, $\Delta\overline{g}_{\text{activn}}$ is the parameter with the most amount of variability. Referring again to Figures 23, when $\Delta\overline{g}_{\text{activn}}$ is less than about 35000 cal/mole, the entire contact interface from 0 to 1.8 mm achieves saturation (i.e., $X_{\text{i}} = X_{\text{i, eq}}$ uniformly). As $\Delta\overline{g}_{\text{activn}}$ increases, X_{i} becomes less than $X_{\text{i, eq}}$ beginning from the cutting edge and moves downstream, but curve fit at the x = 1.8-mm section can still be performed. As mentioned earlier, $\Delta\overline{g}_{\text{activn}}$ can be increased to levels where X_{i} becomes uniformly less than $X_{\text{i, eq}}$ along the contact interface, until it becomes difficult to match the peaks of the concentration profiles of Subramanian et al.

To better estimate the value of $\Delta\bar{g}_{\text{activn}}$, experimental concentration profiles are needed at different distances away from the cutting edge.

The previous discussion is based on the idea that one single profile can be approached spatially in an infinite number of ways. The calibration constant A_0 in Table 4 is also non-unique by at least an order of magnitude, mainly because the rate constant is dominated by the exponential terms. Further non-uniqueness of representation may arise from the non-linear nature of the governing equations. However, restrictions regarding the size of α (Section 3.5.2) and the values of the diffusivities (Section 3.5.1) are expected to hold in all circumstances.

3.8. Notes on the numerical method

The finite element source code is modified from 2D programs for the heat equation taken from the text of Kwon and Bang [2000, Examples 5.9.1 and 6.6.2]. In the 0th-order problem, the main additions are the advection field and coupling between interfacial tool and chip temperatures. In the 1st-order problem, the program is enlarged to model 3 scalar fields that mutually interact through advection, diffusion, and reaction.

In the transient problem of relaxation, X_s cannot be explicitly expressed as an algebraic function of X_i and X_v; hence, it cannot be eliminated as in the steady-state problem. The Newton-Raphson method (Crank-Nicolson time integration with nonlinearity iteration on the solution at the new time step [Zienkiewicz and Taylor, 2000a, pp. 6-8]) proves stable not only for the differing magnitudes of coefficient matrices, but also for handling sharply varying gradients at small regions of the mesh

where wiggles in the solution may be present. Small wiggles are tolerated as a matter of practicality due to the use of the coarsest meshes possible for the quickest solution speeds, but with a compromise in accuracy. In separate tests, wiggles are minimized by local smoothing of any sudden changes in the way k_{diss} varies near the cutting edge, but the impurity profiles and distributions do not show significant changes.

Because the region of interest in the mass-transfer problem measures roughly 0.2 microns by 1800 microns, elements severely elongated in the flow direction (x-direction) have been used. Computationally, the effect is equivalent to neglecting the x-diffusion term, which implies that the relaxation results are only valid for time scales much shorter than that which is necessary for mass-transfer in the flow-direction x. This is deemed acceptable for the geometry considered. Also, in the present case where most boundary conditions are of the flux type, the desired level of mesh refinement to minimize or avoid wiggles can be obtained by trial and error (as opposed to the case of Dirichlet boundary conditions, where limits are placed on the element Peclet number [Gresho and Lee, 1979]).

Chapter 4

CONCLUSIONS AND SUMMARY

In ascribing to the experimental concentration profiles a physical interpretation using the Frank-Turnbull mechanism, we have made use of many assumptions, varied a number of parameters to achieve curve-fit, and calculated quantities that reflect the implications of the model. Here we provide a summary.

4.1. A list of assumptions made, with comments

(1) The work/chip material is assumed incompressible.

Implication: The energy equation does not involve a change in volume term, mainly for simplicity.

(2) Balances of linear momentum and mass are satisfied using the assumptions of classical machining theory. In particular, uniform work and chip flow are assumed sufficient for the present emphasis on high-temperature phenomena.

(3) Bridgman's generalized entropy is assumed for a perfectly plastic work piece.

Implication 1: Accessibility of states via reversible processes is not required.

Implication 2: The stress power $\mathbf{T} : \mathbf{D}$ is completely converted into expelled heat during plastic deformation, which is used to make sense of the meaning of absolute temperature appearing in the energy equation.

Implication 3: The thermodynamic state functions do not depend on kinematic parameters of plasticity, as $\mathbf{T} : \mathbf{D}$ is treated as a heat source.

(4) Weak coupling is assumed between thermal fields and mass-transfer fields, which allows separate consideration of the equations of energy and mass-transfer.

Note: This assumption is justified by the difference in the sizes of thermal and mass diffusivities, but its applicability is limited to regimes where the tool has not worn so much that the background temperature is altered.

Implication: Insular irreversibility [Bridgman, 1950] is limited to the mechanical aspect of the problem governing the background temperature field. A steady temperature field governs the values of constituent solubilities within the chip in the mass-transfer problem.

(5) Chemical equilibrium is invoked in the description of mass transfer—namely, in the phrasing of the boundary flux in terms of the probabilities of tool decomposition and chip-boundary activation.

Note: Our results are consistent with the work of Kramer [1979] in the following sense. The Arrhenius relation enters the flux boundary conditions as probabilities altering the value of the rate constant to the interfacial reaction. In turn, the rate constant governs the speed of rise (spatially and temporally) of the interstitial distribution towards its saturation value. However, the saturation value itself, namely the solubility, is unaffected. As a measure of the maximum amount of dissolution wear possible under all machining conditions, the solubility remains the most important factor.

(6) The order in which the following events occur is immaterial: (i) the system achieving a steady state in global mass transfer, and (ii) the Frank-Turnbull reaction reaching local saturation.

Implication: $\partial(\cdot)/\partial t$ terms and F_S are set to 0 for the time-independent equations.

(7) The concentration profiles of Subramanian et al. are calibrated in our simulations to correspond to a cut section at the end of the contact interface, which is about 1800 microns from the cutting edge. This is the location where the concentration profiles are close to achieving their maximum levels. However, simulation results can be recalibrated to match data at other sections along the tool-chip interface.

(8) The concentrations of defects and impurities are considered small compared to the chip-material concentration, and the total concentration c is assumed constant.

Implication: c is eliminated in the mass transfer equations in favor of mole fraction X, and data from binary phase diagrams can be used directly.

(9) Tracer diffusion is assumed for W and Co within the Fe lattice.

Note: This assumption is made in light of a scarcity of data with ternary and multi-component mixtures [Shewmon, 1989, Section 4.6], but it is fortunately justified by the low concentration levels actually observed.

Implications: diffusivities are independent of impurity concentrations; equilibrium mole fractions of impurities are directly proportional to Arrhenius exponential terms [Shewmon, 1989, Section 2.4]; forcing terms in the species-transfer equations are simplified (Section 3.1).

(10) A vacancy distribution is assumed to rise from a very low value near the interface and jump quickly to a saturation value, mirroring the first rise of the concentration profile of Subramanian et al.

Implication: The assumed vacancy distribution is essential in bringing about the low entry value of X_s before the first rise of the humped distribution, and it reflects the statement that dissolution is "vacancy-controlled for small depth, but interstitial-controlled for large depth."

(11) The Co binder atoms enter the chip region such that the original W-Co molar ratio within the tool is approximately preserved: variations are assumed to be incurred by material loss at the interface.

Justification: That the W-Co molar ratio is approximately preserved is checked directly using experimental profiles (Section 3.4).

Effect on simulations: The solubility of Co is related to the solubility of W by

$$X_{\mathrm{Co,\,eq}} = \varphi X_{\mathrm{W,\,eq}} \quad (\varphi < 1).$$

Implication: Knowing that the cobalt content is restricted by the availability of tungsten within the chip allows the amount of cobalt lost to mechanisms other than dissolution to be estimated.

(12) The W concentration profile is assumed to decay asymptotically to zero and forces the Co concentration profile to vanish along with it (by Assumption 11).

Note: This is simply a modeling decision that frees us from having to impose special assumptions to generate a buildup of X_s at large depths into the chip.

(13) Pressure and damage are two independent ideas that have potential to explain the drastic reduction in the mass diffusivities D_i and D_V from table look-up values.

Note: The drastic reduction in diffusivity values is necessary to maintain a rapidly-rising vacancy distribution and rapidly-decaying interstitial distribution; in turn, the product of these distributions gives rise to the humped X_s distribution that is matched with the experimental data of Subramanian. It is noted that the mass diffusivities used for the two cutting speeds do not differ substantially (Table 4), and are not changed for the post-machining relaxation simulations. This is viewed to be consistent with damage.

(14) Because W and Co have similar atomic radii to Fe, they are assumed to exist more favorably as substitutional impurities rather than interstitial impurities. Hence, $X_{s,eq}$ for W (or Co) is approximately equal to but is less than $X_{W,eq}$ (or $X_{Co,eq}$), whereas $X_{i,eq}$ for W (or Co) is a small remainder, say $\alpha X_{W,eq}$ (or $\alpha X_{Co,eq}$). α happens to be a parameter of curve-fit that directly controls the initial condition of the post-machining relaxation (Figure 20 and its discussion).

(15) The effect of pressure and vacancy concentration on the solubility of interstitials and substitutionals is not expected to change the present results drastically.

Reasoning: X_s is source-limited by the boundary supply of interstitials, or $X_{i,eq}$. Therefore, X_s is of the same order as the maximum of $X_{i,eq}$, implying that $X_s \ll X_{s,eq}$. What is being assumed here is that in spite of changes to $X_{s,eq}$ due to pressure and vacancy concentration, X_s is still

expected to be small in comparison to its ceiling value of $X_{s,eq}$. The parameter of importance is judged to be the curve-fit value of $X_{i,eq}$ at the boundary (viz., the value of α). Error is incurred if changes in $X_{s,eq}$ due to pressure and vacancy concentration are so drastic that the X_s distribution is significantly changed by the changes in the solubility limit.

Implication: $X_{s,eq}$ is based on the solubility of tungsten in iron, which is obtained directly from a W-Fe binary phase diagram without regard to the prevalent pressure and vacancy concentration.

(16) $X_{V,eq}$ is treated as a variable parameter of fitting with experimental data in the absence of an explicit molecular model explaining the formation of vacancies.

(17) The slow decay of X_s is hypothesized to be an effect of relaxation after machining.

Note: Given the constraint of a small value of $X_{i,eq}$, the matching the steady-state X_s distribution to the experimental data has proved difficult. The hypothesis is then developed from the realization that the measured impurity profile is the sum of the steady-state X_s distribution and the residual X_i distribution. Computationally, relaxation gives us one more chance to improve the curve-fit. Physically, a post-machining relaxation actually occurs in the short time between the end of cutting and the quenching of the chips, although the exact time elapsed until quenching has not been reported in the experiments of Subramanian et al [1993].

(18) Interfacial temperature jumps are controlled by the heat-transfer coefficient field, as discussed and justified in Chapter 2 and the Appendix.

4.2. A list of key parameter variations used to achieve match with experimental data

(1) $X_{i,eq}$ (the maximum boundary value of impurity concentration) is chosen so that the residual X_i distribution provides a desired alteration of the X_s decay during the relaxation after the steady-state has stopped. This is controlled by the fraction α in Table 4.

(2) $X_{W,eq}$ and $X_{Co,eq}$ are related by a fraction φ (Section 3.5.4).

(3) $\Delta\bar{g}_{activn}$ mainly controls the variation of X_i along the tool-chip interface, in other words, how much tool components are admitted into the chip lattice. In turn, this affects how X_s varies along the flow direction.

(4) D_i controls the spread of interstitials, and hence the location of the maximum of the X_s distribution; D_V is set so that given a cutting speed, the vacancy distribution applied within the primary shear zone is advected relatively unchanged across the length of the contact interface. These values of diffusivities—much lower than table lookup values—help to achieve the rise and fall of the X_s distribution, the location of its maximum, and its spatial spread.

(5) The saturation value of $X_{V,eq}$ affects the X_s distribution only insofar as it affects the manner in which the $X_{V,eq}$ function rises, but it does not affect the tail of the X_s distribution.

(6) For post-machining relaxation, the value of k_{fwd} determines the rate at which the Frank-Turnbull reaction occurs in relation to the rate of the diffusing interstitial species. A uniform reaction constant k_{fwd} produces fairly good results; improvement is possible if the uniformity of k_{fwd} is not required.

4.3. A summary of motivations, results, and quantities calculated

(1) The functional form of the rate constant k_{diss} for the dissolution of tool constituents inside the chip is obtained by a model of dissolution that is consistent with Kramer's earlier work. Undetermined parameters in the expression for k_{diss} are estimated via a curve-fitting process using the concentration profiles of Subramanian et al. [1993].

(1a) Dissolution is defined as the combined events of tool decomposition at the contact interface and subsequent mass transfer and exchange (advection, diffusion, reaction) into the chip.

(1b) The boundary supply of tool constituents into the chip region is capped by the solubility of tool material within the chip. It is also influenced spatially by Arrhenius terms governing tool decomposition and the jump frequency of tool atoms across the contact interface.

(1c) Low temperatures hinder dissolution. In particular, dissolution wear is decreased wherever the chip interface is cooler due to loose contact.

(2) The dissolved, concentration field within the chip at steady state is calculated using the proposed Frank-Turnbull mechanism, and curve fit is improved using a proposed, mass-transfer relaxation that occurs after cutting.

(2a) The proportions of interstitial impurities and substitutional impurities among the total amount of impurities are given by a curve-fit parameter of the relaxation simulation.

(3) Table-lookup values of diffusivities for W and Co within Fe are too high to achieve a humped concentration profile at the observed space scales. Curve-fit values are used instead, and it is proposed that damage may be the cause for the drastic reductions in diffusivities.

(4) Table-lookup values of the solubility of Co in Fe are too high to achieve the boundary concentration of Co observed. To cap the value of Co solubility, we hypothesize that cobalt remains in roughly equal molar proportions to tungsten before and after cutting.

(5) With information on the amount of WC grains that remain intact after machining [Subramanian et al., 1993, Tables 1 & 2], the proportions of worn cobalt attributed to dissolution mechanisms and non-dissolution mechanisms are estimated.

(6) The functional form of the rate of wear for the tool is given, and it is shown to obey the same variations as the tool-interface temperature.

Appendix

RELATIONSHIP OF INTERFACIAL TEMPERATURE JUMPS TO THE HEAT PARTITION FIELD USING A 1D PROBLEM

A1. Introduction

When one material slides against another, it is commonly assumed that the steady-state temperatures of the two bodies match at their contact interface. In this Appendix, we derive conditions under which interfacial temperature continuity does not hold using a 1D example. The simplicity of the 1D problem allows us to study the cases of an uncoupled interface, an interface obeying temperature continuity, and a convectively cooled interface. It will be shown that when an interfacial-temperature jump does occur, its magnitude can be expressed in terms of the heat partitioned to either side of the interface. Further, for the convectively cooled interface where frictional flux is generated, if the heat partitioned to the work is less than that for the case of temperature continuity, then the work temperature will be cooler than the tool temperature (Inequalities (A24)).

A2. The 1D problem

In Figure A1, the work and tool materials are schematically represented to lie along the x-axis, and they are in contact at the location shared by the work node w2 and the tool node t1:

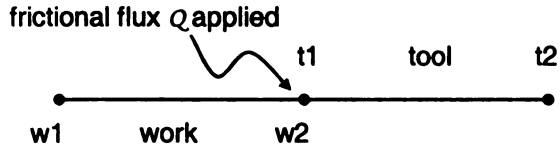

Figure A1: Ideal 1-D representation of the work and tool materials

A heat flux Q (in W/m^2) is applied at the interface. The energy equations governing the work and tool domains are

$$k_{work}\frac{d^2\theta_{work}}{dx^2}-\rho_{work}\hat{c}_{work}v\frac{d\theta_{work}}{dx}=0, \tag{A1}$$

$$k_{tool}\frac{d^2\theta_{tool}}{dx^2}=0. \tag{A2}$$

Here, k is the thermal conductivity, ρ is the density, $\hat{c}$ is the specific heat (per unit mass), v is the cutting speed, θ is the temperature, and x is the distance coordinate. The system is subject to two far-field boundary conditions:

$$\theta_{work}\big|_{x=x_{w1}} = \theta_{w1} = 0, \tag{A3}$$

and

$$\theta_{tool}\big|_{x=x_{t2}} = \theta_{t2} = 0, \tag{A4}$$

the application of which to the solution of Equations (A1) and (A2) yields

$$\theta_{work} = A_w\left[\frac{\exp\left(\frac{\rho_{work}\hat{c}_{work}v}{k_{work}}(x-x_{w1})\right)-1}{\exp\left(\frac{\rho_{work}\hat{c}_{work}v}{k_{work}}L_{work}\right)-1}\right] \quad \text{and} \quad \theta_{tool} = A_t\left(\frac{x_{t2}-x}{L_{tool}}\right). \tag{A5), (A6}$$

Here, A_w and A_t are constants to be determined, $L_{work} = x_{w2} - x_{w1}$, and $L_{tool} = x_{t2} - x_{t1}$. The complete solution (for A_w and A_t) depends on the interfacial conditions applied.

A2.1. The uncoupled interface

At the interface, the conservation of energy requires that

$$k_{work} \left.\frac{\partial \theta_{work}}{\partial x}\right|_{x=x_{w2}} + k_{tool}\left(-\frac{d\theta_{tool}}{dx}\right)_{x=x_{t1}} = Q. \tag{A7}$$

In the absence of additional information on interfacial behavior, the assignment of heat partition is arbitrary. For convenience, an equal partitioning of heat to both work and tool is usually chosen, which is equivalent to the condition

$$k_{work} \left.\frac{\partial \theta_{work}}{\partial x}\right|_{x=x_{w2}} - k_{tool}\left(-\frac{d\theta_{tool}}{dx}\right)_{x=x_{t1}} = 0. \tag{A8}$$

The system of Equations (A1) and (A2), subjected to conditions (A3), (A4), (A7) and (A8), yields an exact solution of

$$\theta_{work} = \frac{Q}{2\rho_{work}\hat{c}_{work}v}\left[\frac{\exp\left(\frac{\rho_{work}\hat{c}_{work}v}{k_{work}}(x - x_{w1})\right) - 1}{\exp\left(\frac{\rho_{work}\hat{c}_{work}v}{k_{work}}L_{work}\right)}\right] \tag{A9}$$

$$\theta_{tool} = \frac{Q}{2k_{tool}}(x_{t2} - x) \tag{A10}$$

As mentioned, the heat partition function β, which for concreteness is defined to be the fraction of heat flowing into the work, is arbitrarily set to 0.5:

$$\beta_{\text{work}} = \beta = 0.5, \tag{A11}$$

$$\beta_{\text{tool}} = 1 - \beta = 0.5. \tag{A12}$$

A2.2. Temperature continuity

The interfacial conditions in this case are

$$\mathrm{k}_{\text{work}} \left.\frac{\partial \theta_{\text{work}}}{\partial x}\right|_{x=x_{\text{w}2}} + \mathrm{k}_{\text{tool}} \left(-\frac{d\theta_{\text{tool}}}{dx} \right)_{x=x_{\text{t}1}} = Q\,, \tag{A13}$$

$$\theta_{\text{work}}\big|_{x=x_{\text{w}2}} - \theta_{\text{tool}}\big|_{x=x_{\text{t}1}} = \theta_{\text{w}2} - \theta_{\text{t}1} = 0\,, \tag{A14}$$

which, together with conditions (A3) and (A4), result in the following exact solution of the system of Equations (A1) and (A2):

$$\theta_{\text{work}} = \left\{ \frac{Q}{\left(\rho_{\text{work}} \hat{c}_{\text{work}} v \left[\frac{\exp\left(\frac{\rho_{\text{work}} \hat{c}_{\text{work}} v}{\mathrm{k}_{\text{work}}} L_{\text{work}} \right)}{\exp\left(\frac{\rho_{\text{work}} \hat{c}_{\text{work}} v}{\mathrm{k}_{\text{work}}} L_{\text{work}} \right) - 1} \right] + \frac{\mathrm{k}_{\text{tool}}}{L_{\text{tool}}} \right)} \cdot \left[\frac{\exp\left(\frac{\rho_{\text{work}} \hat{c}_{\text{work}} v}{\mathrm{k}_{\text{work}}} (x - x_{\text{w}1}) \right) - 1}{\exp\left(\frac{\rho_{\text{work}} \hat{c}_{\text{work}} v}{\mathrm{k}_{\text{work}}} L_{\text{work}} \right) - 1} \right] \right\} \tag{A15}$$

$$\theta_{\text{tool}} = \frac{Q}{\left(\rho_{\text{work}} \hat{c}_{\text{work}} v \left[\frac{\exp\left(\frac{\rho_{\text{work}} \hat{c}_{\text{work}} v}{\mathrm{k}_{\text{work}}} L_{\text{work}} \right)}{\exp\left(\frac{\rho_{\text{work}} \hat{c}_{\text{work}} v}{\mathrm{k}_{\text{work}}} L_{\text{work}} \right) - 1} \right] + \frac{\mathrm{k}_{\text{tool}}}{L_{\text{tool}}} \right)} \cdot \left(\frac{x_{\text{t}2} - x}{L_{\text{tool}}} \right) \tag{A16}$$

Heat partition functions can be calculated from the fluxes evaluated at the interface, and they are

$$\beta = \frac{1}{Q}\left(\mathrm{k}_{\mathrm{work}} \left.\frac{\partial \theta_{\mathrm{work}}}{\partial x}\right|_{x=x_{\mathrm{w}2}} \right)$$

$$= \left(\frac{\rho_{\mathrm{work}}\hat{c}_{\mathrm{work}}\mathrm{v}\left[\dfrac{\exp\left(\dfrac{\rho_{\mathrm{work}}\hat{c}_{\mathrm{work}}\mathrm{v}}{\mathrm{k}_{\mathrm{work}}} L_{\mathrm{work}} \right)}{\exp\left(\dfrac{\rho_{\mathrm{work}}\hat{c}_{\mathrm{work}}\mathrm{v}}{\mathrm{k}_{\mathrm{work}}} L_{\mathrm{work}} \right) - 1} \right]}{\rho_{\mathrm{work}}\hat{c}_{\mathrm{work}}\mathrm{v}\left[\dfrac{\exp\left(\dfrac{\rho_{\mathrm{work}}\hat{c}_{\mathrm{work}}\mathrm{v}}{\mathrm{k}_{\mathrm{work}}} L_{\mathrm{work}} \right)}{\exp\left(\dfrac{\rho_{\mathrm{work}}\hat{c}_{\mathrm{work}}\mathrm{v}}{\mathrm{k}_{\mathrm{work}}} L_{\mathrm{work}} \right) - 1} \right] + \dfrac{\mathrm{k}_{\mathrm{tool}}}{L_{\mathrm{tool}}}} \right), \tag{A17}$$

$$\beta_{\mathrm{tool}} = 1 - \beta = \frac{\dfrac{\mathrm{k}_{\mathrm{tool}}}{L_{\mathrm{tool}}}}{\rho_{\mathrm{work}}\hat{c}_{\mathrm{work}}\mathrm{v}\left[\dfrac{\exp\left(\dfrac{\rho_{\mathrm{work}}\hat{c}_{\mathrm{work}}\mathrm{v}}{\mathrm{k}_{\mathrm{work}}} L_{\mathrm{work}} \right)}{\exp\left(\dfrac{\rho_{\mathrm{work}}\hat{c}_{\mathrm{work}}\mathrm{v}}{\mathrm{k}_{\mathrm{work}}} L_{\mathrm{work}} \right) - 1} \right] + \dfrac{\mathrm{k}_{\mathrm{tool}}}{L_{\mathrm{tool}}}}. \tag{A18}$$

A2.3. Convective cooling

The convective-cooling interface is modeled with a heat-transfer coefficient h as follows. From the work side:

$$\mathrm{k}_{\mathrm{work}} \left.\frac{\partial \theta_{\mathrm{work}}}{\partial x}\right|_{x=x_{\mathrm{w}2}} = \mathrm{h}\left(T_{\mathrm{t}1} - T_{\mathrm{w}2}\right) + \beta Q \tag{A19}$$

From the tool side:

$$\mathrm{k}_{\mathrm{tool}} \left(-\frac{\partial \theta_{\mathrm{tool}}}{\partial x} \right)_{x=x_{\mathrm{t}1}} = \mathrm{h}\left(T_{\mathrm{w}2} - T_{\mathrm{t}1}\right) + (1-\beta)Q \tag{A20}$$

The four conditions (A3), (A4), (A19) and (A20),[13] when applied to the system of Equations (A1) and (A2), yield the following solution, which for simplicity, is given in terms of the constants A_w and A_t of Equations (A5) and (A6):

$$A_w = \theta_{w2} = \frac{\beta \cdot \frac{k_{tool}}{L_{tool}} + h}{\left(h + \frac{k_{tool}}{L_{tool}}\right)\left(h + \rho_{work}\hat{c}_{work}v \cdot \frac{\exp\left(\frac{\rho_{work}\hat{c}_{work}v}{k_{work}}L_{work}\right)}{\exp\left(\frac{\rho_{work}\hat{c}_{work}v}{k_{work}}L_{work}\right)-1}\right) - h^2} \cdot Q \quad (A21)$$

$$A_t = \theta_{t1} = \left(\frac{(1-\beta)\cdot\left(\rho_{work}\hat{c}_{work}v \cdot \frac{\exp\left(\frac{\rho_{work}\hat{c}_{work}v}{k_{work}}L_{work}\right)}{\exp\left(\frac{\rho_{work}\hat{c}_{work}v}{k_{work}}L_{work}\right)-1}\right) + h}{\left(h + \frac{k_{tool}}{L_{tool}}\right)\left(h + \rho_{work}\hat{c}_{work}v \cdot \frac{\exp\left(\frac{\rho_{work}\hat{c}_{work}v}{k_{work}}L_{work}\right)}{\exp\left(\frac{\rho_{work}\hat{c}_{work}v}{k_{work}}L_{work}\right)-1}\right) - h^2} \right) \cdot Q \quad (A22)$$

The equality of the constants A_w and A_t to the interface temperatures of the two regions can be seen by inspection of Equations (A5) and (A6).

From Equations (A21) and (A22), it is seen that setting h = 0 corresponds to the uncoupled-interface solution (Equations (A9) and (A10) with $\beta = 0.5$), while setting h = ∞ corresponds to the temperature-continuity solution (Equations (A15) and (A16)). Hence, the heat transfer coefficient h can be used to describe intermediate behavior; it is presently used to quantify the temperature jump between tool and work:

[13] The case of $Q = 0$ corresponds to flux continuity across the interface and can also be considered; however, the present boundary and interface conditions must be altered for the solution to be non-trivial.

$$A_t - A_w = \theta_{t1} - \theta_{w2}$$

$$= \frac{(1-\beta)\cdot\left(\rho_{work}\hat{c}_{work}v\cdot\frac{\exp\left(\frac{\rho_{work}\hat{c}_{work}v}{k_{work}}L_{work}\right)}{\exp\left(\frac{\rho_{work}\hat{c}_{work}v}{k_{work}}L_{work}\right)-1}\right)-\beta\cdot\frac{k_{tool}}{L_{tool}}}{\left(h+\frac{k_{tool}}{L_{tool}}\right)\left(h+\rho_{work}\hat{c}_{work}v\cdot\frac{\exp\left(\frac{\rho_{work}\hat{c}_{work}v}{k_{work}}L_{work}\right)}{\exp\left(\frac{\rho_{work}\hat{c}_{work}v}{k_{work}}L_{work}\right)-1}\right)-h^2}\cdot Q \qquad \text{(A23)}$$

Since the denominator of the last expression in Equation (A23) is always positive, the inequality

$$\theta_{w2} \le \theta_{t1} \qquad (A24)_1$$

holds as long as

$$\beta \le \frac{\left(\rho_{work}\hat{c}_{work}v\cdot\frac{\exp\left(\frac{\rho_{work}\hat{c}_{work}v}{k_{work}}L_{work}\right)}{\exp\left(\frac{\rho_{work}\hat{c}_{work}v}{k_{work}}L_{work}\right)-1}\right)}{\left(\rho_{work}\hat{c}_{work}v\cdot\frac{\exp\left(\frac{\rho_{work}\hat{c}_{work}v}{k_{work}}L_{work}\right)}{\exp\left(\frac{\rho_{work}\hat{c}_{work}v}{k_{work}}L_{work}\right)-1}+\frac{k_{tool}}{L_{tool}}\right)}. \qquad (A24)_2$$

Note that the right-hand side of Inequality $(A24)_2$ is just the heat partition for the case of temperature continuity (Equation (A17)). Hence, under the assumption of a convective-cooling interface, if the work absorbs less heat than it would have in the case of temperature continuity (Inequality $(A24)_2$), then the work will be at a lower temperature than the tool at the interface (Inequality $(A24)_1$). The precise amount of the temperature

jump is given by Equation (A23). A similar result can be obtained if the direction of the previous inequalities is reversed; namely, $\theta_{w2} \geq \theta_{t1}$ if $\beta \geq$ {right-hand side of $(A24)_2$}.

The heat partition β in the case of convective cooling is viewed as a process parameter that depends on material properties and the details of contact. While β cannot be solved explicitly in the present setup of convective cooling, its limiting behavior can be deduced. Suppose in the steady state, the tool and work temperatures are postulated to match at the interface if the work is stationary, even under convective cooling. In other words, in the limit where v = 0, we set $A_w = \theta_{w2} = \theta_{t1} = A_t$, and from Equation (A23), arrive at

$$\lim_{v \to 0} \beta = \frac{k_{work} / L_{work}}{\left(k_{work} / L_{work} + k_{tool} / L_{tool} \right)}. \tag{A25}$$

On the other hand, as $v \to \infty$, the interfacial temperature jump reduces to

$$\lim_{v \to \infty} A_t - A_w = \lim_{v \to \infty} T_{t1} - T_{w2} = \frac{\left(1 - \lim_{v \to \infty} \beta \right)}{\left(h + \frac{k_{tool}}{L_{tool}} \right)} \cdot Q \geq 0 \text{ whenever } \beta \leq 1. \tag{A26}$$

Note that for temperature continuity, $\lim_{v \to \infty} \beta = 1$ (from Equation (A17)). For the interfacial temperature to drop from tool to work, the condition $\lim_{v \to \infty} \beta < 1$ is needed (for consistency with Inequalities (A24)); the plausibility of such a condition can be shown in the case of a heated object sliding across a cold surface, but will not be pursued here.

A.3. Summary

Using the concept of the heat transfer coefficient, we have concluded that, as long as the heat partitioned to the work is less than that for the case of temperature continuity, then the work temperature will always be cooler than the tool temperature in the 1D problem.

BIBLIOGRAPHY

Ackroyd, B., Akcan, N.S., Chhabra, P., Krishnamurthy, K., Madhavan, V., Chandrasekar, S., Compton, W.D. and Farris, T.N., 2001. "Exploration of Contact Conditions in Machining," *Proceedings of the Institution of Mechanical Engineers, Journal of Engineering Manufacture, Proceedings Part B*, **215**(B4):493-507.

Bird, R.B., Stewart, W.E. and Lightfoot, E.N., 2002. *Transport Phenomena*, 2nd edition. J. Wiley, New York, xii, 895 pages.

Bridgman, P.W., 1950. "The Thermodynamics of Plastic Deformation and Generalized Entropy," *Review of Modern Physics*, **22**(1):56-63.

Chao, B.T. and Trigger, K.J., 1955. "Temperature Distribution at the Tool-Chip Interface in Metal Cutting," *Transactions of the ASME*, **77**:1107-1121 (Discussion pp. 1119-1121).

Chao, B.T. and Trigger, K.J., 1958. "Temperature Distribution at Tool-Chip and Tool-Work Interface in Metal Cutting," *Transactions of the ASME*, **80**:311-320 (Discussion pp. 318-320).

Cook, N.H. and Nayak, P.N., 1966. "The Thermal Mechanics of Tool Wear," *Journal of Engineering for Industry, Transactions of the ASME*, **88**:93-100.

DeVries, W.R., 1992. *Analysis of Material Removal Processes*. Springer Texts in Mechanical Engineering. Springer-Verlag, New York, xvii, 254 pages.

Doyle, E.D., Horne, J.G. and Tabor, D., 1979. "Frictional Interactions between Chip and Rake Face in Continuous Chip Formation," *Proceedings of the Royal Society of London. Series A, Mathematical and Physical Sciences*, **366**(1725):173-183.

Elliott, J.F., Gleiser, M., Ramakrishna, V. and The American Iron and Steel Institute, 1963. *Thermochemistry for Steelmaking, Volume II*. Addison-Wesley Series in the Engineering Sciences - Metallurgy and Materials. Addison-Wesley Publishing Company, Reading, MA

Frank, F.C. and Turnbull, D., 1956. "Mechanism of Diffusion of Copper in Germanium," *Physical Review*, **104**(3):617-618.

Giese, A., Stolwijk, N.A. and Bracht, H., 2000. "Double-Hump Diffusion Profiles of Copper and Nickel in Germanium Wafers Yielding Vacancy-Related Information," *Applied Physics Letters*, **77**(5):642-644.

Gresho, P. and Lee, R.L., 1979. "Don't Suppress the Wiggles-They are Telling You Something." In: T.J.R. Hughes (Editor), *Finite Element Methods for Convection Dominated Flows: Presented at the Winter Annual Meeting of the American Society of Mechanical Engineers, New York, New York, December 2-7, 1979.* AMD (Applied Mechanics Division), v. 34. ASME, New York, N.Y., pp. 37-61.

Hansen, M., (prepared with the cooperation of K. Anderko) and Armour Research Foundation, 1958. *Constitution of Binary Alloys*, 2nd edition. Metallurgy and Metallurgical Engineering Series. McGraw-Hill, New York, 1305 pages (kept up-to-date with two supplements: (1) Rodney P. Elliott and IIT Research Institue, 1965. *Constitution of Binary Alloys. First Supplement*, McGraw-Hill Series in Materials Science and Engineering, New York, 877 pages. (2) Francis A. Shunk and IIT Research Institue, 1969. *Constitution of Binary Alloys. Second Supplement*, McGraw-Hill Series in Materials Science and Engineering, New York, xl, 720 pages. Errata for earlier volumes: pp. xxxv-xxxviii.)

Hautojärvi, P. (Editor), 1979. *Positrons in Solids*. Topics in Current Physics, v. 12. Springer-Verlag, Berlin; New York, xi, 255 pages.

Kim, W. and Kwon, P., 2001. "Understanding the Mechanisms of Crater Wear," NAMRC XXIX, 29th North American Manufacturing Research Conference, University of Florida Hotel and Conference Center, Gainsville, FL.

Komanduri, R. and Hou, Z.B., 2000. "Thermal Modeling of the Metal Cutting Process. Part I - Temperature Rise Distribution due to Shear Plane Heat Source," *International Journal of Mechanical Sciences*, **42**:1715-1752.

Komanduri, R. and Hou, Z.B., 2001a. "Thermal Modeling of the Metal Cutting Process - Part II: Temperature Rise Distribution due to Frictional Heat Source at the Tool-Chip Interface," *International Journal of Mechanical Sciences*, **43**:57-88.

Komanduri, R. and Hou, Z.B., 2001b. "Thermal Modeling of the Metal Cutting Process - Part III: Temperature Rise Distribution due to Combined Effects of Shear Plane Heat Source and the Tool-Chip Interface Frictional Heat Source," *International Journal of Mechanical Sciences*, **43**:89-107.

Kramer, B.M., 1979. *An Analytical Approach to Tool Wear Prediction*. Ph. D. Thesis, Department of Mechanical Engineering, Massachusetts Institute of Technology, 132 pages.

Kramer, B.M. and Judd, P.K., 1985. "Computational Design of Wear Coatings," *Journal of Vacuum Science & Technology A, Vacuum, Surfaces, and Films*, **3**(6):2439-2444.

Kramer, B.M. and Suh, N.P., 1980. "Tool Wear by Solution: A Quantitative Understanding," *Journal of Engineering for Industry, Transactions of the ASME*, **102**:303-309.

Krause-Rehberg, R. and Leipner, H.S., 1999. *Positron Annihilation in Semiconductors: Defect Studies*. Springer Series in Solid-State Sciences, 127. Springer, Berlin; New York, xv, 378 pages.

Kwon, Y.W. and Bang, H., 2000. *The Finite Element Method Using MATLAB*, 2nd edition. CRC Mechanical Engineering Series. CRC Press, Boca Raton, FL, 607 pages.

Mase, G.T. and Mase, G.E., 1999. *Continuum Mechanics for Engineers*, 2nd edition. CRC Press, Boca Raton, FL, 377 p. pages.

Miller, M.K., Cerezo, A., Hetherington, M.G. and Smith, G.D.W., 1996. *Atom Probe Field Ion Microscopy*. Monographs on the Physics and Chemistry of Materials, 52. Clarendon Press; Oxford University Press, Oxford; New York, xi, 4 plates, 509 pages.

Miller, M.K. and Smith, G.D.W., 1989. *Atom Probe Microanalysis: Principles and Applications to Materials Problems*. Materials Research Society, Pittsburgh, Pa., xiv, 278 pages.

Molinari, A. and Nouari, M., 2002. "Modeling of Tool Wear by Diffusion in Metal Cutting," *Wear*, **252**(1-2):135-149.

Naerheim, Y. and Trent, E.M., 1977. "Diffusion Wear of Cemented Carbide Tools when Cutting Steel at High Temperatures," *Metals Technology*, **4**(12):548-556.

Paris, D., Lesbats, P. and Levy, J., 1975. "An Investigation of the Distribution of Vacancies in an Ordered Fe-Al Alloy by Field Ion Microscopy," *Scripta Metallurgica*, **9**:1373-1378.

Rabinowicz, E., 1965. *Friction and Wear of Materials*. Wiley Series on the Science and Technology of Materials. John Wiley & Sons, Inc., New York, 244 pages.

Rabinowicz, E., 1977. "Abrasive Wear Resistance as a Materials Test," *Lubrication Engineering*, **33**(7):378-381.

Rabinowicz, E., Dunn, L.A. and Russell, P.G., 1961. "A Study of Abrasive Wear Under Three-Body Conditions," *Wear*, **4**:345-355.

Shaw, M.C., 1984. *Metal Cutting Principles*. Oxford Series on Advanced Manufacturing (No. 3). Clarendon Press; Oxford University Press, London; New York, xxii, 594 pages.

Shewmon, P.G., 1963. *Diffusion in Solids*. McGraw-Hill Series in Materials Science and Engineering. McGraw-Hill, New York, 203 pages.

Shewmon, P.G., 1989. *Diffusion in Solids*, 2nd edition. Minerals, Metals & Materials Society, Warrendale, Pa., 246 pages.

Sturge, M.D., 1959. "A Note on the Theory of Diffusion of Copper in Germanium," *Proceedings of the Physical Society*, **73**(2):297-306, (journal also known as the *Proceedings of the Physical Society of London* from 1874-1925).

Subramanian, S.V., Ingle, S.S. and Kay, D.A.R., 1993. "Design of Coatings to Minimize Tool Crater Wear," *Surface & Coatings Technology*, **61**(1-3):293-299.

Suh, N.P., 1986. *Tribophysics*. Prentice-Hall, Englewood Cliffs, NJ, xiv, 498 pages.

Tay, A.O., Stevenson, M.G. and de Vahl Davis, G., 1974. "Using the Finite Element Method to Determine Temperature Distributions in Orthogonal Machining," *Proceedings - The Institution of Mechanical Engineers*, **188**:627-638.

Trent, E.M., 1967. "Conditions of Seizure at the Chip-Tool Interface," *Machinability. ISI Special Report 94*. Proceedings of the Conference on Machinability jointly organized by the Iron and Steel Institute and the Institute of Metals, in association with the Institution of Mechanical Engineers, the Institution of Production Engineers, and the Institution of Metallurgists, held at the Royal Commonwealth Society, Craven Street, London WC 2, on 4-6 October 1965, pp. 11-18 (article makes reference to Fig. 13 on p. 182 of the same Proceedings [Trent, "The Relationship between Machinability and Tool Wear," *ibid.*, pp. 179-184]; panel discussion: pp. 55-63).

Wallace, P.W. and Boothroyd, G., 1964. "Tool Forces and Tool-Chip Friction in Orthogonal Machining," *The Journal of Mechanical Engineering Science*, **6**(1):74-87.

Zienkiewicz, O.C. and Taylor, R.L., 2000a. *The Finite Element Method, Volume 2, Solid Mechanics*, 5th edition. Butterworth-Heinemann, Oxford; Boston

Zienkiewicz, O.C. and Taylor, R.L., 2000b. *The Finite Element Method, Volume 3, Fluid Dynamics*, 5th edition. Butterworth-Heinemann, Oxford; Boston

Zorev, N.N., 1958. "Results of Work in the Field of the Mechanics of the Metal Cutting Process," Proceedings of the Conference on Technology of Engineering Manufacture, London: 25th to 27th March, 1958. Session 3, Machining of Materials. Institution of Mechanical Engineers (Great Britain), pp. 255-266, plus Plate 4 (Figs. 54.1a-f), Plate 5 (Figs. 54.7 & 54.9a-b), Plate 6 (Fig. 54.8), & Plate 7 (Figs. 54.18a-b, 54.19, 54.20, & 54.26). Plates (not paginated) are placed between p. 406 and p. 407. Reports, Discussion, Communications, & Authors' Replies for Session 3 are contained in pp. 374-405.